DESIGN OF OPTICAL SKIN PHANTOMS FOR REFLECTION PHOTOPLETHYSMOGRAPHY

A Thesis

by

KEVIN ROBERT BELLOWS

Submitted to the Office of Graduate and Professional Studies of
Texas A&M University
in partial fulfillment of the requirements for the degree of

MASTER OF SCIENCE

Chair of Committee,	Gerard Coté
Co-Chair of Committee,	Kamran Entesari
Committee Members,	Roozbeh Jafari
	Michael Moreno
Head of Department,	Michael McShane

December 2018

Major Subject: Biomedical Engineering

ABSTRACT

Optical interrogation of tissues can be used for monitoring physiological parameters, such as heart rate or heart rate variability, or for diagnosis of disease. One such measurement modality is the photoplethysmogram (PPG), which is common in medical settings but has recently become popular in the general population in the form of fitness trackers. Unlike medical devices which use red and near-infrared light to obtain PPGs, wearable electronics predominantly use green illumination. These optical heart rate monitors are not subject to United States Food and Drug Administration (FDA) regulations because they are classified as low-risk general wellness products. This presents an opportunity for products to be released without being sufficiently tested. Optical phantoms provide a means to test optical systems under controlled conditions without the unpredictability that physiology can impart.

Physical phantom models of blood and skin soft tissue were made with optical agents mixed into water and polydimethylsiloxane (PDMS), respectively, and characterized. Several optical heart rate monitors intended for fitness tracking then underwent testing by being affixed to a skin soft tissue phantom, which had a hollow channel through which the blood phantom was pumped to emulate pulsatile blood flow. The frequency of the pumping waveform was controlled, and the readings from each monitor were compared to this ground truth. A three-axis motion stage was used to test the monitors' abilities to reject motion artifact. Differences in performance between the monitors were observed, which further highlighted the need for *in vitro* testing platforms before sending products to market.

A second generation of skin phantoms was designed to account for the cutaneous microvasculature, which plays an important role in a reflection PPG measurement due to green

light's shallow penetration depth in tissue. Anatomical models describing the layers of the skin and their individual blood content values were analyzed using Monte Carlo simulations. Then, a model with a simplified layered geometry was described and simulated to determine if it could yield a comparable response to that of the anatomical models when considering various epidermis tones.

DEDICATION

To my family.

ACKNOWLEDGEMENTS

Thank you to the chair of my committee, Dr. Gerard Coté, for his guidance and support during the past few years. I also appreciate the time and effort that the co-chair of my committee, Dr. Kamran Entesari, and the other members of my committee, Dr. Roozbeh Jafari and Dr. Michael Moreno, put into helping me during my journey.

Dr. Madeleine Durkee has been indispensable over the course of my work on this research, due to her knowledge of tissue optics, her willingness to talk and to listen, her ability to help me determine what is important and what is not, her vocal faith in me, and her friendship. Dr. Andrea Locke was another source of emotional support when I needed it the most. She is one of the most optimistic, hard-working, and selfless people I know, and she is absolutely willing to share her good energy with all those around her. Dr. Haley Marks shows a passion for optics and for biomedical research that borders on unparalleled. Her enthusiasm is contagious, and I look up to her for that. She also played a very important role in that she gave me the encouragement I needed to join the Department of Biomedical Engineering. Lydia Colvin has quickly cemented herself as an important friend in my life. The conversations and laughter I have shared with her over the past two years have enriched my life. I am thankful to have relationships with each of these colleagues, and I look forward to seeing the amazing ways in which they will undoubtedly continue to build wonderful lives.

Dr. John Choma was one of my favorite professors at the University of Southern California before I began graduate school at Texas A&M University. He trusted in my abilities as an engineering student and quickly became a mentor to me. He was a rarity in the level at which he

cared about his students and their education. He was truly a dedicated man with no ego, and that only added to his brilliance.

One of my biggest sources of support has consistently been Tim Hamilton. He has been unwavering in his encouragement and his empathy in hard times, and he has been incredibly patient while I have been away for so long. He has always been consistent in his desire for me to do what is best for myself, and that is a quality that is truly remarkable, that deserves to be acknowledged, and for which I am thankful. He provides a wonderful example of what it means to live with gratitude.

One of the most difficult aspects of the past few years has been being far away from my family and my home. My brothers, Todd, Scott, and Ryan, are always willing to offer life advice when I need it, for which I am lucky. I appreciate the interest they have shown in my work, and I am looking forward to spending more time with them once I am no longer a flight away.

To my mother, Sharon: You have never let me down. You are always willing to lend an ear, no matter the time, and I appreciate how you have supported me from 1,500 miles away. To my father, Kingsley: You were an honest, honorable, and dignified man, and you were a wonderful example of how to live one's best life. I wish we could share in the joy of my graduation and my return home. Both of you gave Todd, Scott, Ryan, and me a good foundation, life, and family, and for that, I will be forever grateful.

CONTRIBUTORS AND FUNDING SOURCES

This work was supported by a thesis committee consisting of Dr. Gerard Coté (chair), Dr. Kamran Entesari (co-chair), Dr. Roozbeh Jafari (member), and Dr. Michael Moreno (member).

Dr. Madeleine Durkee, a member of Dr. Kristen Maitland's lab, built the integrating sphere system using equipment from her lab, as well as an integrating sphere that belonged to Dr. Michael McShane's lab. Dr. Durkee also provided substantial guidance on phantom fabrication and characterization.

The benchtop system for modeling photoplethysmograms was developed by Dr. Lee Hudson, John Hanks, Dr. Casey Pirnstill, Cody Lewis, and Richard Horner. This system was based on a first-generation system built by Dr. Casey Pirnstill and Dr. Tony Akl.

The initial soft tissue phantom formulations using polydimethylsiloxane (PDMS) were developed by Dr. Tony Akl, Ryan Butcher, and Dr. Casey Pirnstill. Subsequent formulations were developed independently by the student. Dr. Tony Akl, Ryan Butcher, Dr. Casey Pirnstill, Linda Bustaman, and the student worked with incorporating sacrificial sugar structures into PDMS.

All other work for this thesis was conducted independently by the student.

Support for this work came from the Delbert A. Whitaker '65 Analog Fellowship, awarded by the Texas A&M University Department of Electrical and Computer Engineering, as well as from the Texas A&M Engineering Experiment Station (TEES) Center for Remote Health Technologies and Systems.

TABLE OF CONTENTS

Page

LIST OF FIGURES

Page

LIST OF TABLES

NOMENCLATURE

% v/v	volume percent
A	absorbance
a_n	transverse magnetic mode coefficients
AAMI	Association for the Advancement of Medical Instrumentation
b_n	transverse electric mode coefficients
BO09	Black Opal total coverage concealing foundation color #09, “Hazelnut”
BPM	beats per minute
C	molar concentration
c	speed of light
DI H_2O	deionized water
DUT	device under test
ECG	electrocardiogram
FDA	Food and Drug Administration
F_v	volume fraction
g	scattering anisotropy
Hb	hemoglobin
HbO_2	oxyhemoglobin
HHb	reduced hemoglobin
$h_n^{(1)}$	spherical Hankel functions of the first kind
HR	heart rate
HRV	heart rate variability

I	intensity
I_0	illumination intensity
IAD	inverse adding-doubling algorithm
IRB	institutional review board
IS	integrating sphere
j_n	spherical Bessel functions of the first kind
l	path length
L	radiance
LED	light-emitting diode
m	refractive index mismatch
MF42	Max Factor Crème Puff pressed powder color #42, “Deep Beige”
MFP	mean free path
N	number density
n	refractive index
p	scattering phase function
p_{HG}	Henyey-Greenstein phase function
PAT	pulse arrival time
PBS	phosphate-buffered saline
PDMS	polydimethylsiloxane
PEP	pre-ejection period
PPG	photoplethysmogram
PRV	pulse rate variability
PTT	pulse transit time

PWV	pulse wave velocity
Q_s	scattering efficiency
r	radius
$\mathbf{r}$	location
RBC	red blood cell
$R_{baseline}$	baseline reflectance
$R_{diastole}$	reflectance in diastole
$R_{pulsatile}$	pulsatile reflectance
$R_{systole}$	reflectance in systole
RTE	radiative transfer equation
s	distance
$\hat{s}$	direction
SBR	signal-to-baseline ratio
SNR	signal-to-noise ratio
SO_2	oxygen saturation
UV-vis	ultraviolet-visible
x	size parameter
ε	molar attenuation coefficient
θ	scattering deflection angle
λ	wavelength
μ_a	absorption coefficient
μ_s	scattering coefficient
μ_s'	reduced scattering coefficient

μ_t	attenuation coefficient
σ_a	absorption cross-section
σ_{geo}	geometrical cross-section
σ_s	scattering cross-section
φ	azimuthal scattering angle
Ω	solid angle

CHAPTER I

INTRODUCTION

Optical Devices for Physiological Monitoring

At the end of 2016, over 15% of consumers in the United States reportedly owned a smartwatch or fitness band, with similar statistics elsewhere in the world.[1] With their ability to provide physiological data directly to users, wearable devices have become a massive consumer market. Fitbit, Inc. alone sold over 60 million units worldwide between 2012 and 2016,[2] and many of its products feature optical heart rate (HR) monitoring. However, the United States Food and Drug Administration (FDA) classifies such products as low-risk general wellness products, as opposed to medical devices, so long as all claims made by the manufacturers fall within the appropriate guidelines.[3] As a result of this lack of regulation, products that go to market may or may not have been tested adequately to ensure their accuracy across a wide range of scenarios, including being worn by various populations, such as people of different sexes and skin tones. This presents a need for improved testing, both to facilitate better final designs and to accelerate the research and development process.

While an electrocardiogram (ECG) is the gold standard for HR and heart rate variability (HRV) measurements, everyday monitoring for the general public requires a more convenient modality. As an example of the importance of HRV, it has been shown that HRV is decreased from normal 20 minutes before the onset of ventricular tachycardia and that there may be a change in the power spectral density of the HRV 1 hour before onset.[4] During ventricular tachycardia, there is a large HRV and a large variability in the heart beat morphology.[5] Ventricular tachycardia has been linked to an increased probability of sudden death;[6, 7] only 45% of hospitalized patients

with pulseless ventricular tachycardia and no previously documented cardiac arrest rhythms survive until the time of discharge.[7] In hospital settings, ECGs are recorded using several wet electrodes connected directly to the skin, and these monitors are classified as medical devices. However, this form factor is not as convenient or practical outside the hospital as a wristband, and comfort plays a significant role in users' choices. If a wearable device that could seamlessly integrate into a patient's lifestyle that could monitor HRV, then the odds of successful intervention against ventricular tachycardia could increase.

Considering the simpler case of HR monitoring, even when extensive testing is performed on optical monitors on human subjects, there are the problems of lack of controllability and, thus, lack of repeatability. For example, if a wrist-worn monitor performs well on one individual but poorly on another, it is difficult to attribute the change in accuracy to differences in skin tone, strap tightness, monitor location, skin perfusion, pulsatile pressure, motion artifacts, or any other number of parameters over which the researchers do not have precise control. Thus, it may be difficult to determine the best manner in which to modify the hardware or software to improve performance.

Various human studies have been performed to evaluate optical HR monitors. For example, Cadmus-Bertram et al. studied four commercially available fitness watches on 40 healthy adults and found that the 95% limits of agreement of the monitors with an ECG ranged from approximately ±5 beats per minute (BPM) to approximately ±10 BPM during rest and from about ±25 BPM to about ±40 BPM during the exercise portion of the study.[8] Wang et al. similarly evaluated four fitness watches against an ECG on 50 healthy subjects.[9] 14% of the subjects were African American, though there is no aggregated data presented describing the skin tone distribution of the subjects, which affects light-tissue interactions. This study found the monitors

to perform better with the subjects at rest than during exercise, and the 95% limits of agreement ranged from about ±25 BPM to about ±35 BPM for the various products. No disparities were observed as a result of body mass index, age, or sex, though, again, no analysis regarding skin tone is provided. However, the standards set for by the Association for the Advancement of Medical Instrumentation (AAMI) stipulates that HR meters for medical use must have a range of at least 30 BPM to 200 BPM (and up to 250 BPM for children) and must have an error that is ≤10% or ≤5 BPM, whichever is larger.[10]

There are some sensors that do meet the criteria to be regulated as medical devices. In fact, significant research efforts continue in optical diagnosis and monitoring of disease. Similar to optical HR monitors, many of these sensors probe information about the pulse itself, as in the case of hemodynamic monitors.

Photoplethysmography

A photoplethysmogram (PPG) is a light-based measurement wherein the amount of blood in a tissue is indirectly assessed based upon the principle of light absorption. PPGs can be obtained in either reflection or transmission mode, with different advantages of each. Transmission mode PPG monitors capture light that has traveled through a larger amount of tissue than reflection mode monitors, which means the pulsatile amplitude of the PPG signal will be larger, as well. However, transmission measurements are limited to body locations and wavelengths such that a sufficient amount of light is able to reach the photodetector without being absorbed or reflected out of the illuminated side of the tissue. Reflection mode PPG monitors have a degree of depth selectivity based on the wavelength of light used for illumination, since different wavelengths will have different penetration depths. PPG measurements can be taken on various body locations, such as the finger, wrist, liver, or small intestine. The underlying principle of PPG measurement is the

same in all cases, however: increased local blood volume causes increased light absorption and decreased detected intensity.

PPG sensors are commonly found in doctor's offices and hospitals, particularly in the form of fingertip pulse oximeters. These devices use the difference in spectral absorption coefficient between two forms of hemoglobin (Hb), oxyhemoglobin (HbO_2) and reduced hemoglobin (HHb), which are the most prominent forms in healthy individuals. By capturing PPGs with two or more wavelengths of light, typically 660 nm and 940 nm,[11] a system of equations can be formed to estimate the ratio of HbO_2 to total Hb, which is known as the oxygen saturation (SO_2). Since HbO_2 absorbs 660 nm light less strongly than HHb and HbO_2 absorbs 940 nm light more strongly than HHb, the overall absorption of 660 nm light decreases and the overall absorption of 940 nm light increases as SO_2 increases.[11, 12]

In addition to probing different forms of Hb, PPG sensors can be used to measure the HR and HRV of an individual.[13] Since the arteries and arterioles distend during systole, the phase of the cardiac cycle when the heart pumps, and recoil during diastole, the phase of the cardiac cycle when the heart relaxes, the local blood volume repeatedly increases and decreases. By analyzing the period of these fluctuations in local blood volume, these physiological parameters can be determined.

One disadvantage of monitoring HRV via PPG instead of ECG is the mismatch between the true pulse rate variability (PRV) that occurs in the blood vessels and the true HRV, as based on an ECG. The PRV has been shown to differ from the HRV at respiratory frequencies[14] and that the difference between the two metrics is correlated with the pulse transit time (PTT), the time taken for the pressure pulse to travel from one location to another.[14, 15] When studying healthy males, Bulte et al. found a high correlation between HRV and PRV but that the PRV overestimated

the high-frequency HRV.[16] Furthermore, Pinheiro et al. found that PRV was a suitable surrogate for HRV in healthy subjects but questionable for subjects with cardiovascular disease or who were post-exercise.[17]

There have also been significant research efforts toward developing cuffless blood pressure (CBP) monitors based solely on the information found in multiple PPG measurements or on the information found in ECG and PPG measurements.[18-21] Such research focuses on the pulse wave velocity (PWV), which is the speed at which the pressure pulse propagates through the arterial tree, as well as waveform features. PWV values in humans range from 4 m/s to 15 m/s.[22] (The speed of the pulse wave is different than the speed of the blood itself, which is on the order of 0.2 m/s.)[22] The PWV can be equivalently expressed as a PTT, assuming the distance traveled through the arteries between measurement sites is well-known. Alternatively, the pulse arrival time (PAT), which is the time between the R-peak of the ECG and the arrival of the next pressure wave at a PPG measurement location, is frequently used as a basis for CBP measurements instead of PTT. PAT-based techniques have the distinct advantage of a long propagation time due to the long distance between the heart and a typical PPG measurement location, such as the wrist or a finger. This relaxes the time resolution requirements since small errors are insignificant relative to large values. However, the mathematical theory behind PWV relates specifically to wave propagation within the blood vessels, whereas PAT measurements inherently include the pre-ejection period (PEP), which is the delay between the electrical R-peak of the heart and the subsequent mechanical pumping of blood out of the left ventricle and into the aorta. Though they measure much shorter delay times, PTT monitors ignore the PEP and have the very practical advantage of having more comfortable, convenient form factors, which may lead to improved adoption and adherence to monitoring protocols.

Optical Phantoms for Modeling and Testing

In vitro systems afford improved controllability at the expense of simplified anatomical and physiological models. Optical phantoms are materials can be used to model the optical properties of tissues and, thus, be used as consistent testing platforms for multiple design iterations. For example, a bulk tissue can be modeled by a solid material fabricated in a laboratory with the proper optical properties. Then, blood can be modeled by a solution or suspension in liquid. In order to generate a HR signal with these materials, a pump can be used to modulate the flow and pressure within openings in the bulk tissue, analogous to the heart pumping blood through the arterial tree. Optical phantoms have been used extensively in the literature. For example, they have been used to model tissues under various conditions, such as changes in perfusion or oxygenation,[23, 24] and to model tissue for imaging purposes.[25] Of particular importance is the ability of phantoms to model tissue under typical or common conditions, as well as in more extreme corner cases in which sensor or device failure may be more likely. This allows devices to be evaluated over a broad range of physiological values and thus exposes any weaknesses.

CHAPTER II

TECHNICAL BACKGROUND

Tissue Optics

Descriptions of Optical Parameters

Since PPGs depend on light-tissue interactions, there are several wavelength-dependent optical parameters that form the basis of their operation. The refractive index n is an indicator of the speed of light in a medium and is given by

$$n \equiv \frac{c_0}{c_{medium}} \tag{1}$$

where $c_0 \approx 3\text{x}10^8$ m/s is the speed of light in vacuum and c_{medium} is the speed of light in the medium of interest.

One possible interaction between light and tissue is absorption. The probability of this phenomenon is described by the absorption coefficient μ_a, which has dimensions of inverse length. The reciprocal of the absorption coefficient gives the mean path length traveled by a photon before being absorbed. The intensity of light I that exists after traveling some path length l in a purely absorbing medium with constant μ_a and an illumination intensity of I_0 is given by (2).

$$I = I_0 e^{-\mu_a l} \tag{2}$$

For a single absorbing species, the absorption coefficient is related to the number density N of the species by

$$\mu_a = \sigma_a N \tag{3}$$

where σ_a is the absorption cross-section of this species.

This gives direct rise to the Beer-Lambert law, which states that the absorbance A of a nonscattering medium with a single purely absorbing species of molar attenuation coefficient ε and molar concentration C as in (4).

$$A \equiv \log\left(\frac{I_0}{I}\right) = \varepsilon c l \tag{4}$$

From (2), (3), and (4), the absorption coefficient can be determined to be

$$\mu_a = \ln(10)\varepsilon c = \ln(10)\frac{A}{l} \tag{5}$$

for a single species. Expanding this to mixtures of several species yields

$$\mu_a = \ln(10)\sum_i \varepsilon_i C_i = \sum_i \sigma_{a,i} N_i = \ln(10)\frac{A}{l} \tag{6}$$

where each value of i designates a different species. In blood, the main absorbing species is Hb, including both HbO_2 and HHb; in the epidermis, the main absorber is melanin. For a mixture where each value of i designates a different absorbing medium, the absorption coefficient is given by

$$\mu_a = \sum_i \mu_{a,i} F_{v,i} \tag{7}$$

where F_v is the volume fraction of the medium in the overall mixture.

Another process which can occur as a result of light-tissue interactions is scattering, which is the redirection of a photon into a new direction. Scattering events can be elastic or inelastic. Inelastic scattering phenomena such as Raman scattering and Brillouin scattering are very weak phenomena and thus do not need to be considered in relation to PPGs. Elastic scattering events, in which the energy of the photon remains unchanged, are described by the scattering coefficient μ_s. Similar to the absorption coefficient, the scattering coefficient has dimensions of inverse length and is a measure of the probability of a scattering event occurring. The reciprocal of the scattering

coefficient is the mean distance a photon travels between scattering events. When an infinitesimally narrow collimated beam of light is shone through a scattering medium with zero absorption, the intensity of the unscattered beam after a path length l is

$$I = I_0 e^{-\mu_s l} \tag{8}$$

where I_0 is again the illumination intensity.

Similar to μ_a for a single absorbing species, μ_s for a medium with a single scattering species is related to its scattering cross-section σ_s by (9).

$$\mu_s = \sigma_{s,i} N_i \tag{9}$$

For a mixture of scattering species, each described by a unique index i, the overall scattering coefficient is given by (10).

$$\mu_s = \sum_i \sigma_{s,i} N_i \tag{10}$$

For a mixture where each value of i indicates a unique scattering medium, the scattering coefficient is given by (11).

$$\mu_s = \sum_i \mu_{s,i} F_{v,i} \tag{11}$$

Equations (2) and (8) can be combined to describe the intensity of an infinitesimally narrow collimated beam of light in a medium that is both absorbing and scattering.

$$I = I_0 e^{-(\mu_a + \mu_s) l} = I_0 e^{-\mu_t l} \tag{12}$$

In (12), μ_t is the attenuation coefficient and is the sum of μ_a and μ_s. The reciprocal of the attenuation coefficient is the mean free path (MFP), which is the mean path length between interactions with the medium, as shown in (13).

$$MFP = \frac{1}{\mu_t} = \frac{1}{\mu_a + \mu_s} \tag{13}$$

Scattering can be isotropic or anisotropic. In the case of isotropic scattering, the scattering deflection angle θ, which is the polar angle, has a uniform probability distribution over its range of [0, π] radians; for anisotropic scattering, θ has a nonuniform distribution. The scattering anisotropy g is defined as the mean cosine of the deflection angle, as in (14).[26, 27]

$$g \equiv \langle \cos\theta \rangle = \int_{4\pi} p(\theta) \cos\theta \, d\Omega = \int_0^{\pi} p(\theta) \cos\theta \cdot 2\pi \sin\theta \, d\theta \tag{14}$$

Here, the scattering phase function p is the probability density function of the deflection angle and Ω is a solid angle. The cases of isotropic scattering, completely forward scattering with a constant $\theta = 0$, and completely backward scattering with a constant $\theta = \pi$ correspond to a g value of 0, 1, and −1, respectively. μ_s and g can be combined into a single parameter, the reduced scattering coefficient μ_s', given in (15).

$$\mu_s' = \mu_s (1 - g) \tag{15}$$

μ_s describes the scattering on a single-scattering level, whereas μ_s' describes the scattering on a multiple-scattering level. The reciprocal of μ_s' is the effective mean distance between a point where a photon is propagating in a particular direction and the point where the photon has lost that directional information. μ_s' is useful for describing media that are turbid enough to scatter photons many times each. It has been noted that μ_a and μ_s' are sufficient to approximate the fluence rate in the diffusion regime in a medium that is homogeneous and whose optical properties do not depend on a photon's direction, though there is an exception at boundaries.[28] For this reason, when preparing models of radiative transfer in the diffusion domain, a model with slightly inaccurate μ_s and g which balance out to yield an accurate μ_s' will be a better representation than a model with accurate μ_s and inaccurate g (or vice versa) to yield an inaccurate μ_s'.

Rather than being represented by a simple weighted average of the g values of its constituent species, the scattering anisotropy of a mixture of various spherical scattering particles is given by (16), where each value of i indicates a different scattering species.[29]

$$g = \frac{\sum_i \sigma_{s,i} g_i N_i}{\sum_i \sigma_{s,i} N_i} \tag{16}$$

When considering a mixture of scattering media with spherical scattering particles, rather than the constituent scattering particles themselves, the scattering anisotropy is described by

$$g = \frac{\sum_i \mu_{s,i} g_i F_{v,i}}{\sum_i \mu_{s,i} F_{v,i}} \tag{17}$$

where each value of i indicates a different scattering medium.

Mie Theory

Elastic scattering occurs when a particle is surrounded by a medium and the two have mismatched refractive indices. Elastic scatterers can be described as one of two main types: Rayleigh scatterers or Mie scatterers. Rayleigh scattering occurs when a scattering particle is much smaller than the wavelength of light, and the scattering cross-section and scattering coefficient in this case are proportional to λ^{-4}. As the scattering particle's size approaches the light's wavelength, the scattering falls under the category of Mie scattering. (Technically, Rayleigh scattering is an approximation of Mie scattering in which the particle size is much smaller than the wavelength.) Scattering coefficients due to Mie scattering have a much flatter spectrum than those due to Rayleigh scattering. Mie scattering is also an anisotropic process, whereas Rayleigh scattering is generally taken to be isotropic. The scattering phase function is well-approximated by the Henyey-Greenstein phase function p_{HG}, shown in (18).[27]

$$p_{HG}(\theta) = \frac{1}{4\pi} \frac{1-g^2}{\left(1+g^2-2g\cos\theta\right)^{3/2}} \tag{18}$$

Mie theory, derived from Maxwell's equations, describes the scattering characteristics (cross-section and anisotropy) of particles with particular geometries in a medium, such as spheres or cylinders. Here, spherical particles are considered, and their scattering characteristics are described by spherical harmonics. Two sets of functions form the foundation of this analysis: the spherical Bessel functions of the first kind j_n and the spherical Hankel functions of the first kind $h_n^{(1)}$.

The two parameters that determine the particle's scattering characteristics are the refractive index mismatch m between the scattering particle and its surrounding medium and the size parameter x, which are defined in (19) and (20), respectively.[26]

$$m \equiv \frac{n_{particle}}{n_{medium}} \tag{19}$$

$$x \equiv \frac{2\pi n_{medium} r_{particle}}{\lambda_0} \tag{20}$$

$r_{particle}$ is the radius of the spherical scattering particle, and λ_0 is the wavelength of light in vacuum. Assuming the permeability of the scattering particle is equal to that of the surrounding medium, the transverse magnetic mode coefficients a_n and the transverse electric mode coefficients b_n are given as follows.[26]

$$a_n = \frac{m^2 j_n(mx)\left[x j_n(x)\right]' - j_n(x)\left[mx j_n(mx)\right]'}{m^2 j_n(mx)\left[x h_n^{(1)}(x)\right]' - h_n^{(1)}(x)\left[mx j_n(mx)\right]'} \tag{21}$$

$$b_n = \frac{j_n(mx)\left[xj_n(x)\right]' - j_n(x)\left[mxj_n(mx)\right]'}{j_n(mx)\left[xh_n^{(1)}(x)\right]' - h_n^{(1)}(x)\left[mxj_n(mx)\right]'} \tag{22}$$

The scattering cross-section of a sphere can then be calculated with (23).[26]

$$\sigma_s = \frac{2\pi}{\left(\frac{2\pi n_{medium}}{\lambda_0}\right)^2} \sum_{n=1}^{\infty} (2n+1)\left(|a_n|^2 + |b_n|^2\right) \tag{23}$$

The scattering efficiency, defined in (24) as the ratio between a particle's scattering cross-section and geometrical cross-section σ_{geo}, is used to calculate the anisotropy factor g of a spherical Mie scatterer in (25).[26]

$$Q_s \equiv \frac{\sigma_s}{\sigma_{geo}} = \frac{\sigma_s}{\pi r_{particle}^2} \tag{24}$$

$$g = \frac{4}{x^2 Q_s}\left[\sum_{n=1}^{\infty} \frac{n(n+2)}{n+1} \mathrm{Re}\left\{a_n a_{n+1}^* + b_n b_{n+1}^*\right\} + \sum_{n=1}^{\infty} \frac{2n+1}{n(n+1)} \mathrm{Re}\left\{a_n b_n^*\right\}\right] \tag{25}$$

Since many components of tissue are on the scale of wavelengths in the visible spectrum, including cells, organelles, and filamentous protein structures, tissue exhibits extremely anisotropic scattering characteristics, often with $g > 0.8$. The scattering cross-section is also quite high due to the large number density of such structures.[30]

Monte Carlo Modeling

In order to understand photon transport in a given medium, mathematical modeling is essential, since the irradiance in a three-dimensional volume is difficult to quantify in physical structures. The principle of radiative transfer is governed by the radiative transfer equation (RTE). The time-independent version of the RTE for monochromatic light is given in (26).[27]

$$\frac{\partial L(\mathbf{r},\hat{s})}{\partial s} = S(\mathbf{r},\hat{s}) - \mu_t L(\mathbf{r},\hat{s}) + \mu_s \int_{4\pi} L(\mathbf{r},\hat{s}')\, p(\hat{s},\hat{s}')\, d\Omega' \tag{26}$$

The RTE states that the change in radiance L at location $\mathbf{r}$ in direction $\hat{s}$ with respect to distance s is due to gain S of radiance from sources, like illumination or fluorescence; loss of radiance through interactions with the medium, namely absorption or scattering into a new direction; and a gain of radiance due to scattering from other directions $\hat{s}'$ into the direction $\hat{s}$, the magnitude of which is dependent on the scattering phase function p from $\hat{s}'$ to $\hat{s}$.

The RTE has analytical solutions when certain assumptions are met, such as in the case of the diffusion domain, but it has no analytical solution in general. Monte Carlo modeling is a powerful stochastic tool that allows statistical predictions of photon paths and irradiance by simulating the interactions of many photons with the medium, using wavelength-specific and location-dependent refractive index, absorption coefficient, and scattering coefficient as inputs. Monte Carlo simulations can provide crucial insight into photon transport otherwise unavailable. A summary of the procedure used to simulate photon transport in the software developed by Wang et al. is shown below in Figure 1.[31]

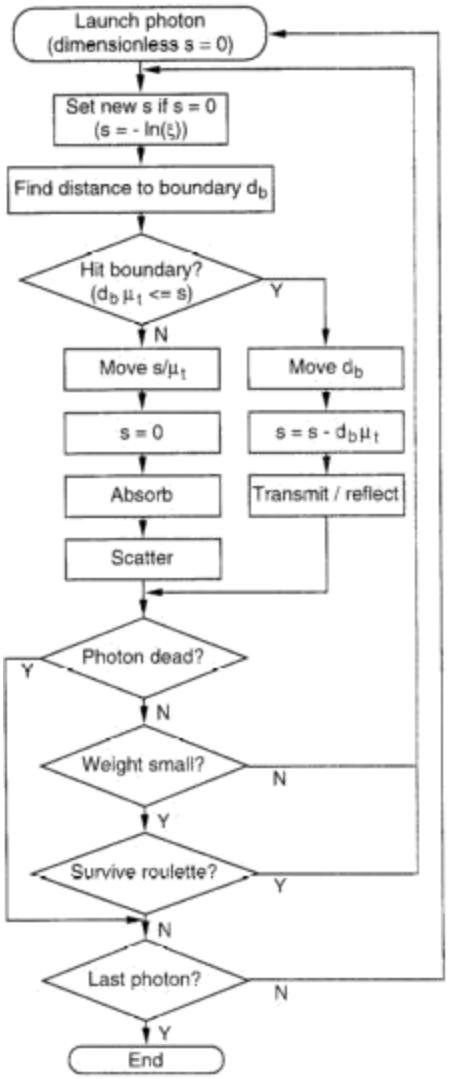

Figure 1. Flowchart describing the algorithm used in the multilayered Monte Carlo simulator. Reprinted from *Computer Methods and Programs in Biomedicine*, **47**(2), L. Wang, S. L. Jacques, and L. Zheng, "MCML—Monte Carlo modeling of light transport in multi-layered tissues," 131-146, 1995 with permission from Elsevier. http://www.sciencedirect.com/journal/computer-methods-and-programs-in-biomedicine

Wang et al. implemented the following procedure in their computer program.[31, 32] Throughout the process, each photon packet's location and direction of propagation are tracked. A photon packet of unity weight is launched orthogonally toward the tissue. A decision is made probabilistically as to whether the photon packet undergoes specular reflection or propagates into the tissue. Based on μ_t, a statistical distribution of the free path is calculated, which is the distance

traveled s. A value of the free path is chosen randomly based on this distribution, and the photon packet is moved one free path in the direction of propagation. Then, a portion of the photon packet's weight is absorbed, and the remaining weight is scattered, with θ chosen by the Henyey-Greenstein scattering phase function in (18) and the azimuthal scattering angle φ chosen from a uniform distribution over the interval $[0, 2\pi]$. Then, the new direction of propagation is calculated, and a new free path is randomly chosen. When an interface between two layers is reached, the photon packet is either reflected or transmitted, again with each interaction having the appropriate probability, which is based on the refractive indices of the two layers in question, as well as the angle of incidence. If the photon packet exits the tissue, it is terminated. Alternatively, if the weight is very small ($<10^{-4}$), a roulette is implemented to randomly choose in an unbiased manner whether to terminate the photon packet.

Spectroscopic Characterization Techniques

Ultraviolet-Visible Absorbance Spectroscopy

As mentioned in (6), the absorption coefficient of a nonscattering material is directly proportional to its absorbance. The only other measurement necessary to deduce μ_a is the path length l, which, in a purely absorbing material, is identical to the sample's thickness. Thus, to determine μ_a in the visible spectrum, ultraviolet-visible (UV-vis) absorbance spectroscopy can be used.

In order to measure the absorbance at a specific wavelength, a monochromator must be used either on the illumination or on the transmitted light. (Assuming the amount of photoluminescence to be either relatively small or zero eliminates the need for two monochromators, one before and after the sample, and allows the use of just one.) Since scattering

will affect an absorbance measurement, μ_a can only be determined in this method for samples that have negligible scattering in the wavelength range of interest.

Integrating Sphere Measurements and Inverse Adding-Doubling Algorithm

For scattering samples, with either zero or nonzero μ_a, optical characterization can be performed by taking measurements with an integrating sphere (IS) and processing the resultant data, such as running it through an inverse adding-doubling algorithm (IAD), to determine μ_a, μ_s', and, if desired, μ_s and g. There are other was to process the data, such as by using Kubelka-Munk theory or the diffusion approximation of the RTE, but IAD was the method used in this work. A system can contain more than one IS, but only a single IS is considered here.

An IS is a hollow sphere that is coated with a highly reflective material on its inner surface, often barium sulfate or Spectralon, and a few ports that form holes in its surface: an entry port, an exit port, and a detection port that is connected to a fiber and a spectrometer or other type of photodetector. An IS has the unique ability to capture light in a broad solid angle, as opposed to more common optics like lenses or optical fibers that are more limited in the light they can collect, since the reflective inner wall will keep photons contained with little chance of absorption. Thus, photons will typically continue to reflect off the wall until reaching the detection fiber. Though different photons will take different amounts of time to finally reach the fiber, a constant radiance at the entry port sets up a steady state situation.

For characterizing optical samples, such as tissues or phantoms, with an IS and IAD, a narrow beam of collimated illumination is ideal. To characterize the system before measuring a sample, four types of measurements must be performed. First, the exit port is capped and the illumination itself is measured by shining it directly into the IS. Then, the same configuration is used with no illumination to measure the noise floor of the system. A stray light measurement is

performed in which the illumination is shone into the IS and the exit port is uncapped. This allows any light that is captured by the IS due to imperfect collimation or alignment to be accounted for later. Finally, a reflectance standard is placed against the uncapped exit port to measure the response due to a known reflectance value. Two additional measurements must be performed on the sample itself. First, a transmission measurement is performed in which the sample is placed against the entry port with the exit port capped. Then, a reflection measurement is performed in which the sample is placed against the uncapped exit port. These six measurements, along with the sample thickness, sample n, parameters of the glass slides surrounding the sample (if used), and geometrical and optical parameters of the IS are enough to run IAD.

Scattering anisotropy can also be determined by IAD if a third sample measurement is performed without the IS. A narrow, collimated beam of light is passed through the sample, with a pinhole and photodetector aligned but far away. This setup will capture the unscattered transmitted light (ballistic photons), which can be normalized to the illumination measured with no sample in the path to determine the sample's unscattered transmittance. In this case, it is especially important to use a very thin sample if it is heavily scattering to improve the intensity at the photodetector. If the sample is too thick, the photodetector's reading will not be distinguishable from zero. As an alternative to performing this additional measurement, g can be determined mathematically, such as with Mie theory as previously described, or by goniophotometry, in which collimated light is shone orthogonal to the surface of a very thin sample and the angular distribution of the transmitted photons is measured. If g is determined by either of these latter two methods, it can be specified as an input to IAD; otherwise, IAD will assume $g = 0$.

IAD[33] works by guessing μ_a, μ_s', and g for a single wavelength and computing the transmittance, reflectance, and unscattered transmittance values associated with those parameters,

along with sample thickness and refractive index, glass slide thickness and refractive index, and IS parameters. If there is a mismatch between the calculated transmittance and reflectance, then μ_a, μ_s', and g are adjusted and the transmittance, reflectance, and unscattered transmittance are recalculated. This process is repeated until the calculated values converge to the measured values, and then the parameters for the next wavelength are determined. Through this procedure, tissue samples can be characterized and thus used as references for optical phantoms to model.

CHAPTER III

DEVELOPMENT OF SINGLE-VESSEL SKIN PHANTOMS

Illumination Spectra of Considered Optical Heart Rate Monitors

Many optical HR monitors for fitness tracking utilize green light to collect reflection PPGs. To illustrate the typical wavelengths used in these devices, the normalized illumination spectra of several commercial HR monitor products and/or commercial HR monitor prototypes are shown below in Figure 2. Since the range of wavelengths at or above half of the maximum intensity for the light-emitting diodes (LEDs) found in these products falls into the range of approximately 490 nm – 560 nm, this was the wavelength range for which the skin phantoms were designed. Characterization metric goals, discussed later, were defined at the center of this range, 525 nm.

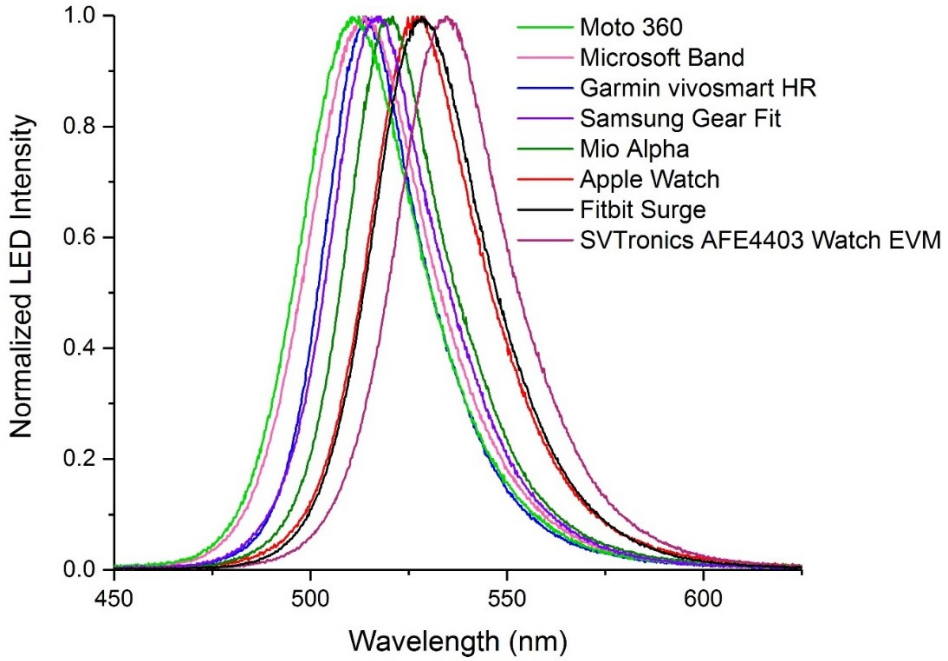

Figure 2. Normalized illumination spectra of several commercial HR monitor products and/or commercial HR monitor prototypes.

Optical Properties of Whole Blood

The molar attenuation coefficient of HbO_2 and HHb are shown below in Figure 3 as a function of wavelength.[12] The normal concentration of Hb in human whole blood is reported as different ranges, but the range given by diagnostic testing company Quest Diagnostics[34] is shown below in Table 1, along with the range for anemia as described by Otto et al.[35] In light of these values, the blood phantom was designed to model the optical properties of whole blood with a Hb concentration of 150 g/L. Since Hb has a small diameter of approximately 5 nm,[36] it can be taken to have negligible scattering properties; its ε shown in Figure 3 can be attributed entirely to absorption. The absorption spectra of oxygenated whole blood and deoxygenated whole blood in the visible range were assumed to be due entirely to HbO_2 and HHb, respectively, and are shown below in Figure 4. Since the concentration of Hb in blood does vary between individuals and even within a single individual over time, there was some tolerance for error in the blood phantom's optical properties.

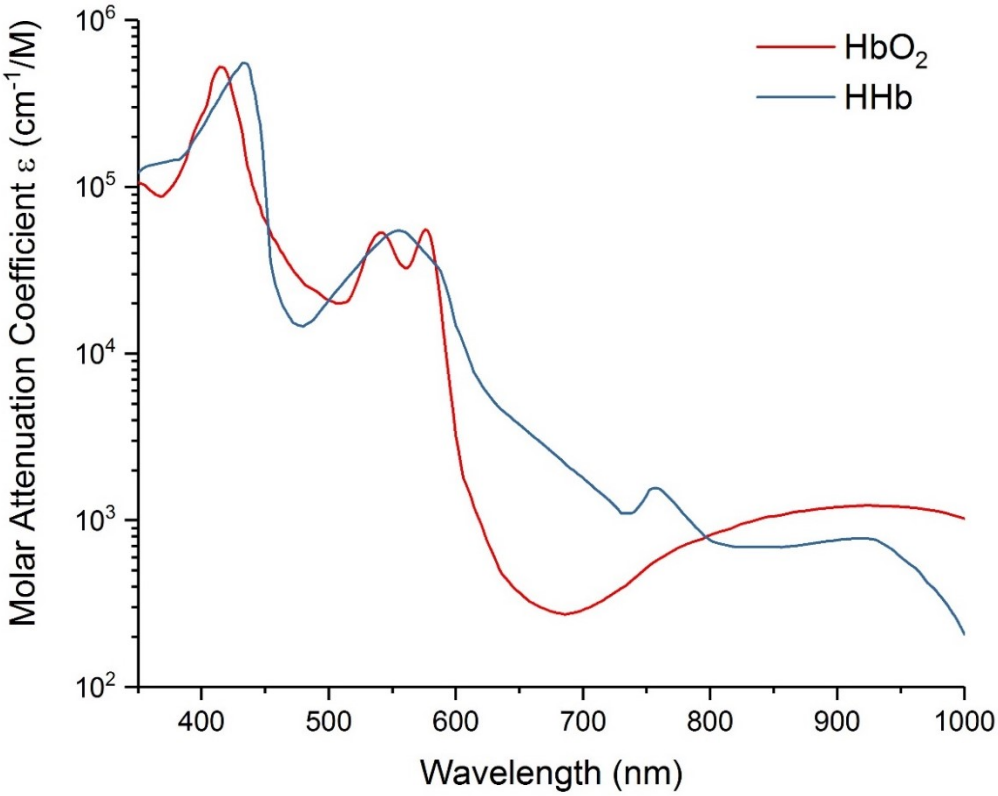

Figure 3. Molar attenuation coefficient as a function of wavelength for HbO_2 and HHb.[12]

Table 1. Reference values for the concentration of Hb in human whole blood.

Hb Concentration in Whole Blood	Normal Range[34] (g/L)	Anemic Range[35] (g/L)
Adult females	117–155	< 120 (non-pregnant)
Adult males	132–171	< 130

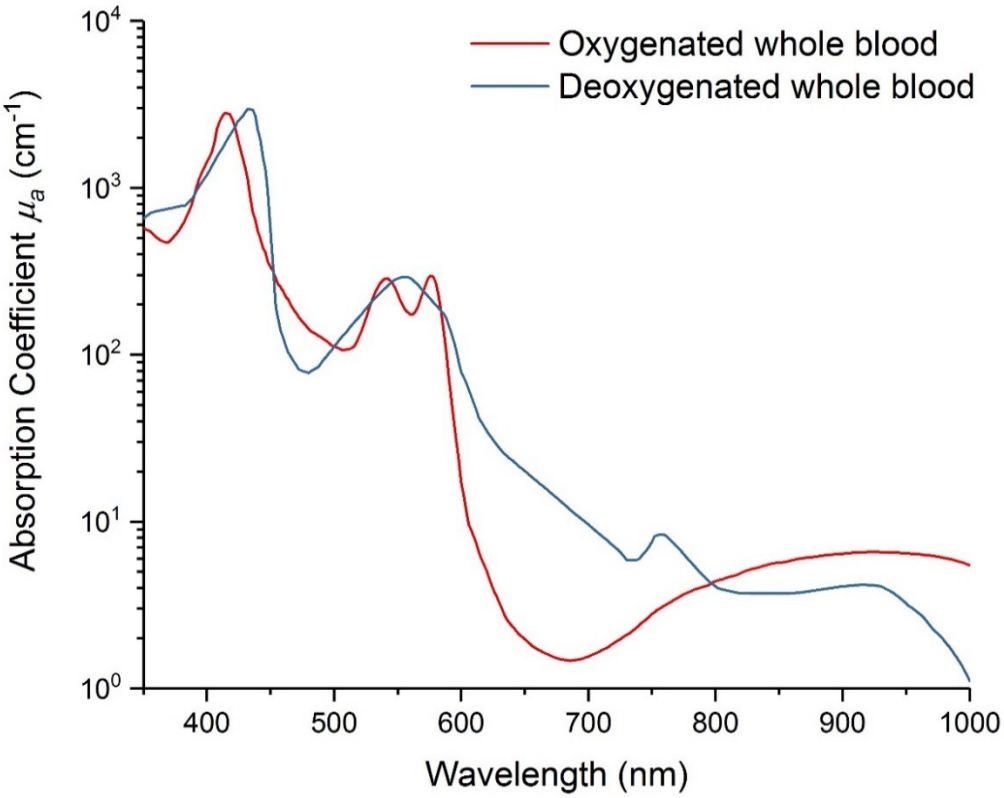

Figure 4. Absorption coefficient of oxygenated whole blood and deoxygenated whole blood. These values assume a Hb concentration of 150 g/L.

The scattering properties of whole blood, modeled and approximately calculated by Faber et al.,[37] are shown below in Table 2, and the refractive index of blood was reported as approximately 1.345–1.350 by Nahmad-Rohen et al.[38] μ_s and, as a result, μ_s' are dependent on the number density of red blood cells (RBCs), which is related to the hematocrit, so the μ_s' values in Table 2 are estimates.

Table 2. Estimated scattering properties of whole blood.[37]

Blood Oxygenation State	**λ (nm)**	**μ_s' (cm^{-1})**	***g***
Oxygenated	525	18.42	0.9954
Deoxygenated	525	15.51	0.9958

Development of Blood Phantom

Attempts to incorporate Al_2O_3 scattering particles of different diameters into DI H_2O had limited success due to sedimentation. However, since μ_s' is much smaller than μ_a for both oxygenated whole blood and deoxygenated whole blood, μ_s' was less important to model in the blood phantom. Thus, a nonscattering fluid was used as the blood phantom.

In order to model the blood with a blood phantom, appropriate absorbers needed to be placed in solution at the proper concentrations. Since the refractive index of blood is ~1.345–~1.350,[38] DI H_2O (n = 1.33) and phosphate-buffered saline (PBS) were both appropriate solvents. In the wavelength range of 490 nm – 560 nm, there is not a major difference in μ_a of HbO_2 and HHb. However, for wavelengths between 600 nm and 800 nm, μ_a is much larger for HHb than for HbO_2. Typically, different phantoms are needed to model oxygenated blood and deoxygenated blood. However, due to the similar values of μ_a in the case of green light, a single phantom was used to mimic blood, regardless of its oxygenation state. This is especially useful since the tissue volumes probed by green illumination on the surface of the skin include arterioles, capillaries, and venules, the blood within each of which can be represented with a single common solution.

Though the absorbance spectra of some dyes change when they are dissolved in PBS versus DI H_2O, this shift was small when observed during blood phantom development. As a result, either of these solvents can be used. As described in (5), the absorbance, measured via traditional UV-vis absorbance spectroscopy, can be used to calculate μ_a of a purely absorbing medium.

Several dyes were investigated to determine their potential for modeling the absorption characteristics of whole blood. Among these dyes were crystal violet, acid violet 17 (dye content 50%), Congo red, tartrazine (a yellow dye), India ink, and various food dyes. The spectra of acid violet 17 and tartrazine had the best overlap with the spectrum of oxygenated blood, so, these two

dyes were combined in the blood phantom. The absorption coefficients of each of these two dyes at varying concentrations in DI H_2O are shown below in Figure 5.

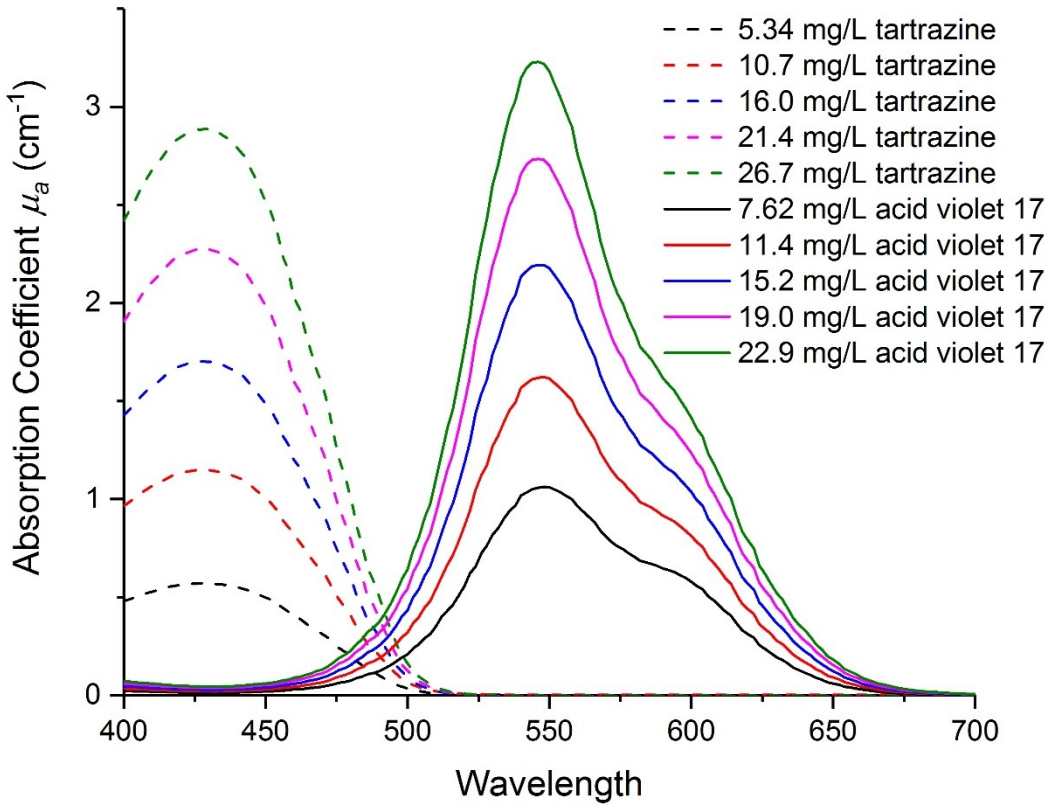

Figure 5. Absorption spectra of tartrazine and acid violet 17 in DI H_2O.

For a phantom modeling light transport in the 490 nm to 560 nm range, tartrazine and acid violet 17 were selected as the best dyes to model oxygenated or deoxygenated blood. Since these two dyes have overlapping spectra, several combinations of concentrations were tested to determine the best solution to model the absorption coefficient of blood. The final blood phantom formulation is shown in Table 3, and the absorption coefficient of this mixture across wavelength is plotted against those of oxygenated whole blood and deoxygenated whole blood in Figure 6.

Table 3. Formulation of blood phantom in DI H_2O.

Dye	Concentration (mg/mL)
Acid violet 17 (dye content 50%)	2.1439
Tartrazine	8.4218

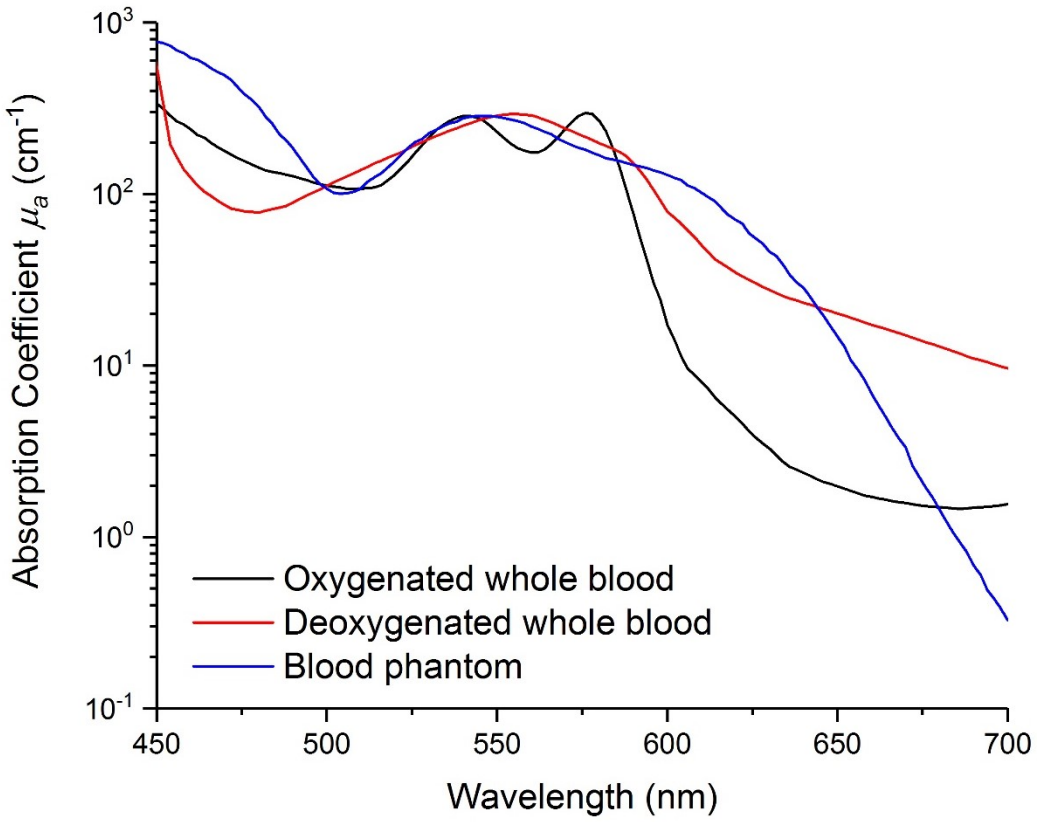

Figure 6. Absorption coefficient of blood phantom compared to those of oxygenated whole blood and deoxygenated whole blood.

Optical Properties of Skin and Development of Initial Soft Tissue Phantoms

The optical properties of Caucasian skin and the tissue preparation methods used on the measured samples were obtained from the literature in order to provide target ranges for a soft tissue phantoms. The data sets considered here were the results of measuring whole skin and are

shown in Table 4. These optical properties cannot be measured *in vivo* because accurately measuring the transmittance with an IS using green illumination requires a skin thickness that is thinner than what is found on the body. Thus, the skin must be removed before it can be characterized. The optical properties, however, are changed as a result of sample removal and preparation.[30] For example, changes in blood content will affect the measured values. While storing the samples in saline may keep the tissue at a physiological hydration level, if the level of hydration during storage is incorrect, the measured properties may have some error relative to the *in vivo* case.[30] In addition, the IAD method itself contributes some error to the optical property values, and error in the IAD inputs of transmittance and reflectance can yield much larger error in the optical property outputs.[33] For example, Prahl et al. noted that for a particular set of IAD input values, the error in the computed μ_a due to IAD was 1% but that when changing the transmittance and reflectance values by 1%, the new computed μ_a had an error of 17%.[33]

Table 4. Tissue preparation methods and optical properties of Caucasian skin as found in the literature. The values presented here were obtained from published plots and thus may have some error relative to the original data sets. M: mean.

Tissue Type	**Tissue Preparation Method**	**Sample Size**	**λ (nm)**	**μ_a (cm^{-1})**	**μ_s' (cm^{-1})**	***g***
Caucasian skin[39, 40]	Stored in saline at ~20 °C; measured one day after autopsy.	21	525	1.139 (M)	28.97 (M)	Not given
Female Caucasian skin[40, 41]	Harvested from buttocks or back of the leg within 24 hours of death; contained epidermis and partial dermis.	1	525	4.638	22.42	Not given

The soft tissue phantoms developed in this work were made with polydimethylsiloxane (PDMS), an elastomer that is well-suited for rapid prototyping. Specifically, Sylgard 184 (Dow

Corning Corporation, Midland, MI) was used. Two components, the base and the curing agent, were mixed together in a mass ratio of 25 to 1 and allowed to crosslink, a process which occurs at room temperature but can be accelerated by placing the mixture in an oven. PDMS itself is optically clear, so μ_a, μ_s', and g are determined by the substances that are added into the mixture before crosslinking has occurred. Specifically, optical agents were thoroughly mixed in with one Sylgard 184 component, after which the remaining Sylgard 184 component was added and stirred in manually until the mixture looked homogeneous. After thorough mixing, the base was added and stirred in manually until the mixture looked homogeneous. The homogeneity was important to ensure the phantom materials had consistent optical properties across the entire sample. Second, since the optical agents started off only in the curing agent and the clear base was added later, homogeneity indicated that the base and the curing agent were well-mixed and would thus crosslink properly. After mixing, the PDMS was poured into the desired mold, degassed using a vacuum chamber, and placed in an oven at 80 °C to cure. The faster the steps after mixing were performed, the less sedimentation was able to occur of optical agents in the phantoms before being immobilized in the cured PDMS.

The initial soft tissue phantom developed in this work to represent light skin was developed with foundation makeup—Max Factor Crème Puff pressed powder color #42, "Deep Beige" (MF42) (Coty, Inc., New York City, NY)—and Al_2O_3 particles (Inframat Advanced Materials, Manchester, CT), a combination which has been used in skin phantoms in the past.[42] The Al_2O_3 particles had a median diameter in the range of 0.5 μm – 1 μm. The initial soft tissue phantom developed to mimic medium skin contained Black Opal total coverage concealing foundation color #09, "Hazelnut" (BO09) (BioCosmetic Research Labs, New York City, NY) and the same Al_2O_3 particles as the light phantom. The concentration of each optical agent used is shown below in

Table 5. These optical agents were added to the Sylgard 184 base, and the mixture was sonicated for several hours to aid in breaking up any clumps of particles, stopping to stir manually after every hour of sonication. Foundation makeup has the advantage of being designed to match the appearance of skin across the visible spectrum, and the Al_2O_3 was used to add additional scattering. However, tuning μ_a and μ_s' for these phantom materials was made difficult by the fact that foundation makeup has absorbing and scattering characteristics, so adjusting its concentration had stronger consequences than if it were a pure absorber. Characterization of both of these skin phantoms was performed by measuring a slab of each formulation with an integrating sphere (Edmund Optics, Barrington, NJ). The system consisted of a white halogen light (Ocean Optics, Largo, FL), a spectrometer (Ocean Optics, Largo, FL), and reflectance standards, which provided calibration measurements for 10% reflectance and 50% reflectance (Labsphere, North Sutton, NH). The results of this characterization are also shown in Table 5.

Table 5. Formulations and optical properties for initial soft tissue phantoms.

Soft Tissue Phantom	**Concentration of MF42 (mg/g PDMS)**	**Concentration of BO09 (mg/g PDMS)**	**Concentration of Al_2O_3 (mg/g PDMS)**	**μ_a (cm^{-1}) at 525 nm**	**μ_s' (cm^{-1}) at 525 nm**
Light	24.1	0	14.9	6.703	60.59
Medium	0	24.1	23.2	24.04	40.07

μ_a of the light soft tissue phantom was slightly higher than that of the more absorbing skin sample described in Table 4, and μ_a of the medium soft tissue phantom was much more absorbing than both skin samples. In contrast to this desired behavior, the μ_s' values yielded by characterizing the soft tissue phantoms were above what was seen in the *in vivo* samples. Another problem in this experiment was that the process to determine the μ_a and μ_s' values of these PDMS materials had

some errors. First, the samples that were measured on the IS were too thick. The light PDMS and the dark PDMS samples were 1.48 mm and 0.90 mm thick, respectively, and their transmittance in the 490 nm – 560 nm range was < 1.5% and < 2.5%, respectively, with their transmittance at 525 nm being ~0.4% and ~1%, respectively. A more reliable calculation of optical parameters would have been possible with higher transmittance values. In addition, the stray light in the IS was assumed to be zero rather than being measured, which was almost assuredly an incorrect assumption. Finally, IAD was designed to have the reflectance calculated with respect to that of a standard, and the algorithm corrects for nonlinearities in the collected signal due to the IS.[43] However, the reflectance values that were input to IAD were calculated from a linear calibration developed with two different reflectance standards of reflectance values 10% and 50%. While this likely reduced the nonlinearity in the reflectance value, IAD was still operating under the assumption that the nonlinearity had not yet been corrected for. The magnitude from this error was likely fairly small, but when combined with the problem of low transmittance, the overall error associated with the IAD output could have compounded.

Though the scatterers present in the makeup could be gathered from the ingredients lists, which mention talc, TiO_2, and $CaCO_3$ for MF42 and silica and TiO_2 for BO09, their size distributions and concentrations were unknown. This meant that the values of *g* of MF42 in PDMS and of BO09 in PDMS could not be calculated with Mie theory. Thus, it was unknown whether the scattering anisotropy of these soft tissue phantoms was close to what is found *in vivo*, as determining it experimentally would require either an unscattered transmittance measurement in conjunction with the IS measurements and IAD or goniometer measurements, both of which are difficult techniques to perform.

These two soft tissue phantoms were each cured with a metal rod in them, which was then removed afterward. The resulting soft tissue phantom was a single, optically homogeneous piece of PDMS with a hollow channel running through it laterally, visible in Figure 7 below. This hollow vessel was then connected to tubing at its inlet and its outlet, which allowed blood phantom to fill and be pumped through the channel. This configuration was meant to model the time-varying local blood volume due to arterial pulsatility. In particular, using a mass ratio of Sylgard 184 base to curing agent of 25 to 1 achieved a lower crosslinking density and yielded a more compliant vessel than using the manufacturer-recommended ratio of 10 to 1 would have. However, the model's anatomical relevance suffered due to the size of the artery. The mean radial artery is approximately 2.2–2.5 mm in diameter and 2 mm below the surface of the skin.[44, 45] While the channels in these soft tissue phantoms were 2 mm deep, they were 6.35 mm in diameter. In addition, the entire solid portion was a model of the optical properties of bulk skin, rather than having multiple layers, as is the case *in vivo*. However, this initial prototype offered a proof of concept that skin phantom systems can be used to test optical HR monitors for such performance parameters as steady state accuracy, latency, and transition rate of output, as shown in the following chapter.

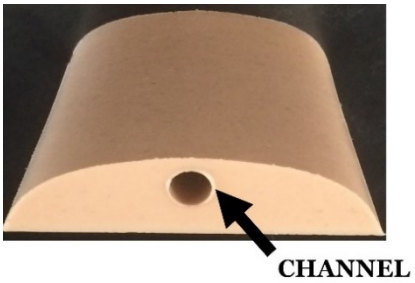

Figure 7. Photograph of the light single-vessel soft tissue phantom.

CHAPTER IV

IN VITRO GENERATION OF PHOTOPLETHYSMOGRAPHIC SIGNALS IN SINGLE-VESSEL SKIN PHANTOMS

Benchtop System for Modeling Photoplethysmograms

The purpose of developing optical phantoms is to ultimately use them in the design and testing of products that depend on the optical behavior of relevant tissues. In particular with PPGs, the signal comes from a variation in the optical power captured by a photodetector. In order to emulate this property of being dynamic, the physical form of a phantom meant for PPG testing must be able to change over time in a controllable fashion. In order to achieve this, a pump was used to push blood phantom through the solid portion of the skin phantom. The pump was thus acting like a heart in that it was generating flow through a channel or network, as well as causing a resultant pressure wave and distension of the compliant walls. The driving voltage waveform controlling the pump was given the same shape as a PPG signal captured *in vivo* from an individual with light epidermis. This data collection was part of a protocol approved by the Texas A&M University institutional review board (IRB), study #IRB2014-0299D. With a pump-based benchtop system, the parameters of the *in vitro* signal can be adjusted. One of these such parameters is the frequency of the signal, which is analogous to the HR. Additionally, the magnitude of the optical signal can be adjusted by changing the Young's modulus of the solid portion of the skin phantom, the pulsatile amplitude at which the pump runs, or both. A schematic of the system used in this work is shown in Figure 8.

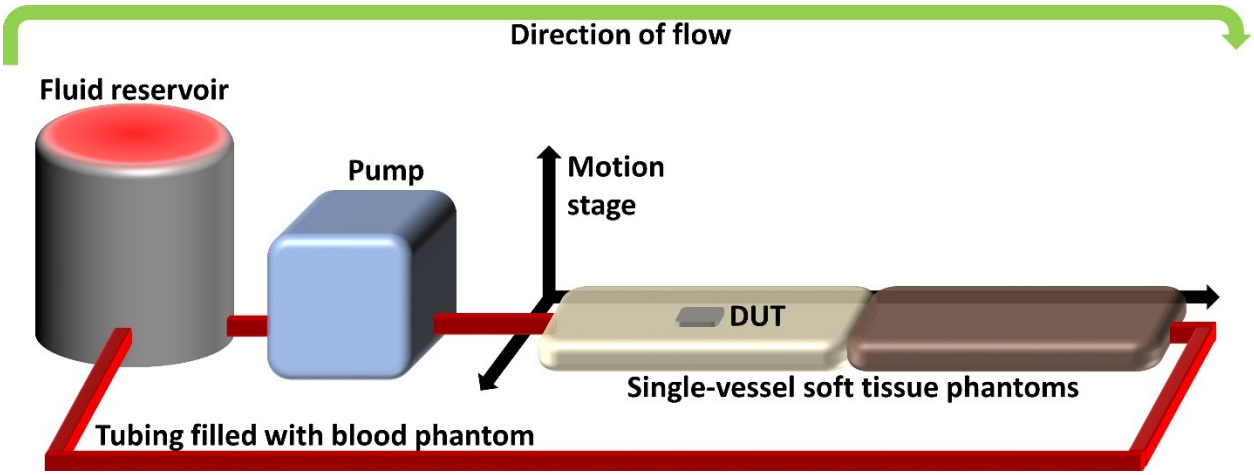

Figure 8. Benchtop system for generating PPG waveforms *in vitro*. DUT: Device under test.

Comparative Test of Various Heart Rate Monitors *In Vitro*

The benchtop system for generating PPG waveforms was utilized in a HR monitoring application. Four commercial HR monitor products and/or commercial HR monitor prototypes that used green illumination were tested on the single-vessel light skin phantom whose optical properties were shown in Table 5. Attempts were made to test on the single-vessel medium skin phantom, but no readings were given by the monitors. Even though the two phantoms were measured to have similar μ_a and μ_s' values, the medium skin phantom was much darker than the light one—a photograph of the two skin phantoms and the benchtop system is in Figure 9. The medium phantom's inability to yield an interpretable PPG signal is evidence that this particular physical model does not sufficiently represent photon transport in tissue and indicates a need to adjust the model.

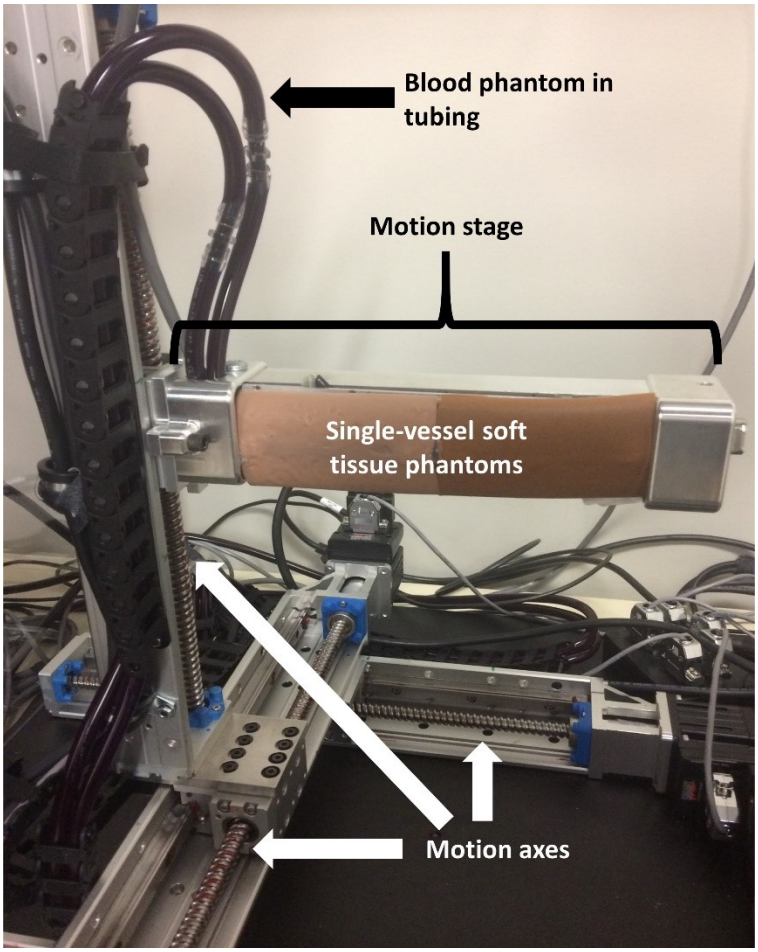

Figure 9. Photograph of the *in vitro* PPG waveform generation system.

Two tests were carried out on each HR monitor, both while the three-axis motion stage emulated a jogging motion to introduce motion artifact. First, a constant-frequency PPG signal was generated by the pump to model a constant HR, shown in Figure 10 as a thick black line. The monitors were strapped onto the skin phantom somewhat loosely to allow for large motion artifact. Device under test (DUT) 1 and DUT 4 performed well during this test, staying within ±1 BPM of the input value. DUT 2 started off near the correct value but slowly drifted farther away. DUT 3 gave correct readings for part of the test but has a period of approximately a minute and a half where it completely lost the signal before eventually recovering.

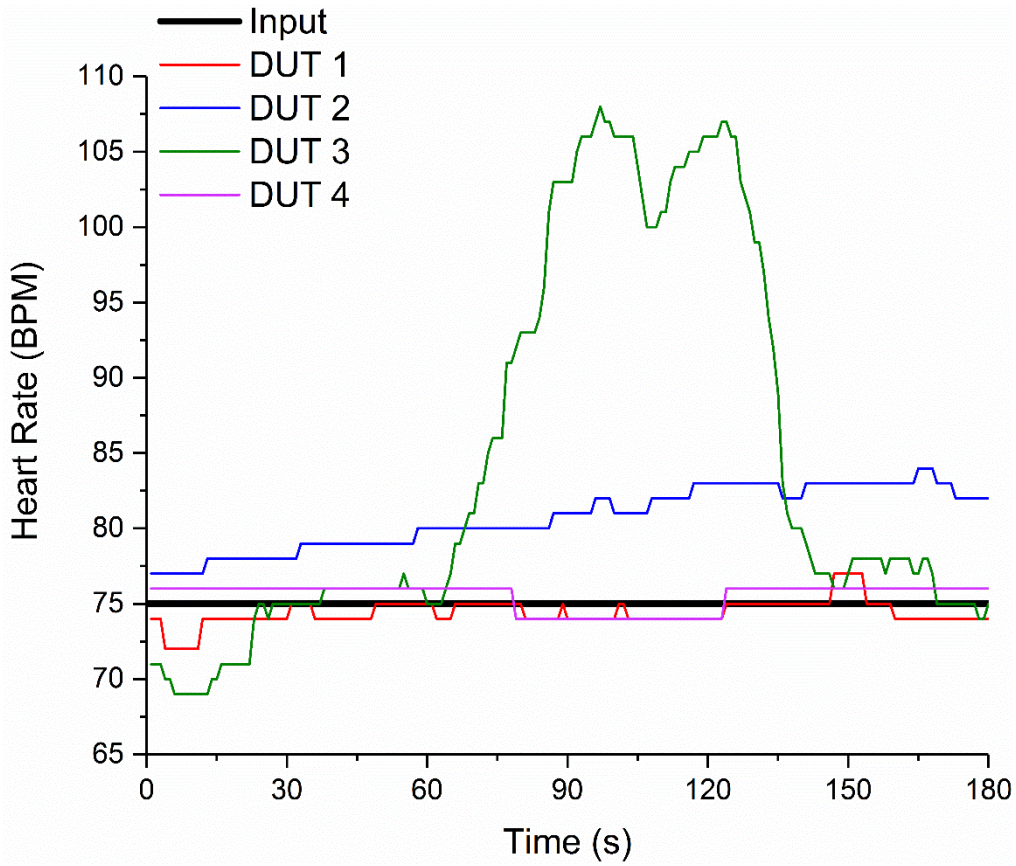

Figure 10. Results of the *in vitro* PPG test with constant HR input.

During the second test, the results of which are shown in Figure 11, the monitors were strapped tightly to the skin phantom to decrease the motion artifact. A staircase input HR profile was used in which an abrupt change in the HR occurred every minute. By using an input that changed rapidly, the monitors' response times were able to be compared, along with their ability to reach the correct steady state value. DUT 1 was clearly the most successful monitor with accurate steady state readings for the first eight minutes, short lags after HR changes in HR, and extremely abrupt, accurate transitions from one HR to another when necessary. DUT 2 performed reasonably well but did not have the same transition slope exhibited by DUT 1. DUT 4 performed well at times and did not give readings at other times. Since the readings it gave were mostly very

accurate, it is possible that crossing a particular threshold of uncertainty causes the monitor to issue no reading rather than risk giving incorrect information. DUT 3 again showed poor performance, with its reading being seemingly random for the first four minutes of the test, followed by accurate readings before losing track of the signal at the end.

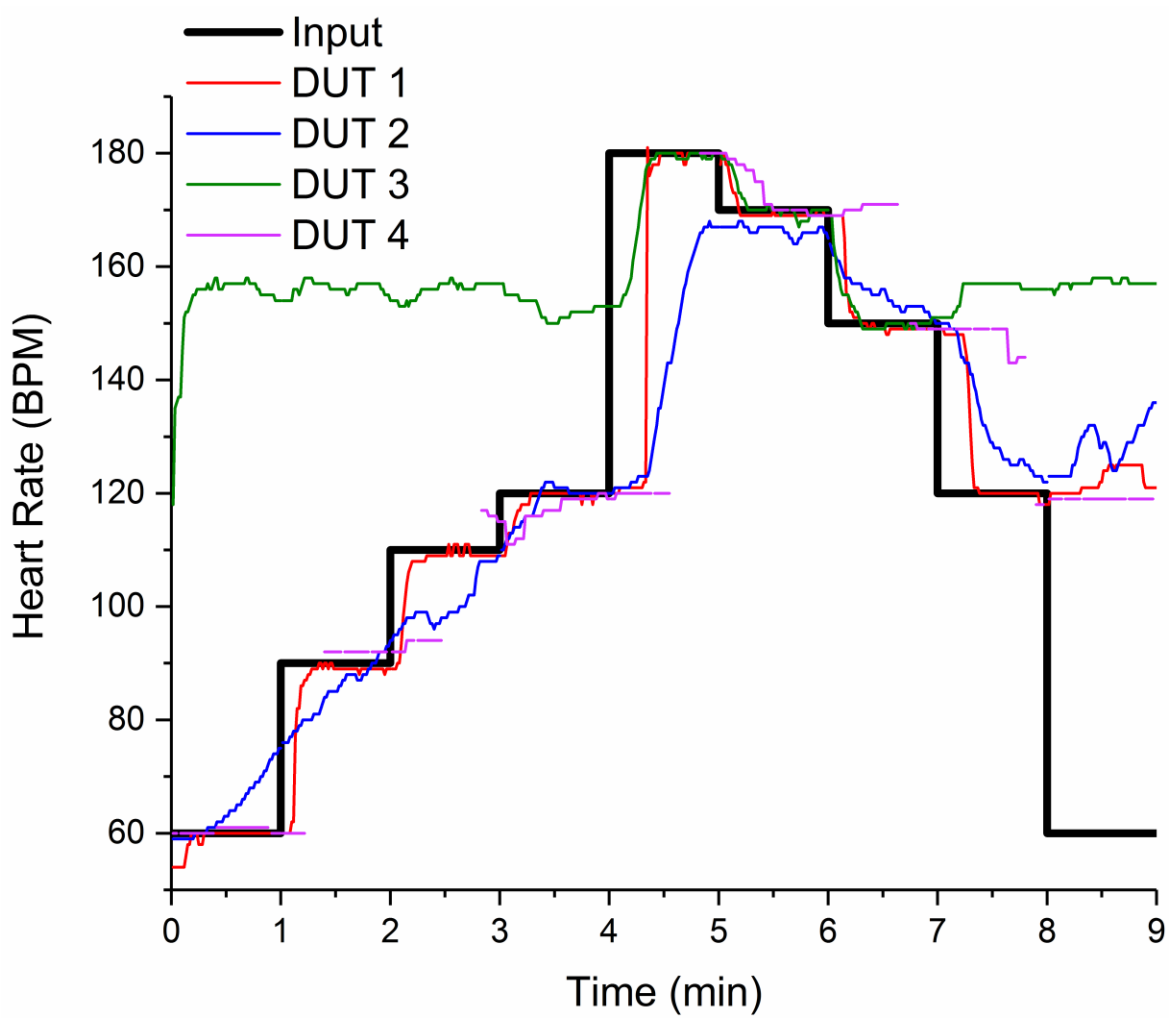

Figure 11. Results of the *in vitro* test with staircase HR input.

The successful recognition of HR values from the pump by some of the DUTs indicates that these products do have some ability to monitor HR if the optical signal is sufficiently large and that the phantom system is capable of generating physiologically relevant PPG waveforms.

While differences in performance by various monitors show a potential for phantom systems to be used to inform changes to the hardware, the software, or both to improve robustness to the monitors with poorer performance, the failure experienced by some HR monitors cannot be doubtlessly assigned to product quality over inaccuracies in the physical model used in this experiment. In particular, due to the shallow penetration depth of green light in skin tissue, models whose time-varying physical attributes are only found starting 2 mm below the surface are questionable in their ability to correctly describe the *in vivo* condition. Thus, a better depth resolution of the optical properties was required.

CHAPTER V

MODELING THE SKIN WITH GREATER SPATIAL RESOLUTION

Structure of the Skin

The skin is made up of an outer layer of epidermis, with a layer of dermis lying beneath it, followed by a layer of tissue called the hypodermis, the subcutaneous tissue, or the subcutis.[46] Values of average blood content in the dermis vary in the literature. Zonios et al. used modeling to fit their measured data and determined that the Hb content in the skin on the back of 10 subjects ranged from 22 mg/L to 41 mg/L.[47] Comparing this to the reference Hb concentration in blood[34] of 150 g/L yields an average blood content of 0.0147 volume percent (% v/v) to 0.0273% v/v. According to a review paper by Lister et al.,[30] various researchers have used values of 2% v/v, 2.6% v/v, or 12% v/v of blood in the skin in their anatomical models. The extreme lack of consensus on this topic makes modeling light transport in the skin a difficult task.

With a wavelength that does not penetrate deep into the skin tissue, such as the 525 nm light considered here, however, the spatial distribution of blood becomes more important than the overall average concentration because the penetration depth is not large enough for photons to visit the entire volume. As a result, it was important to consider the complex nature of the microvasculature in skin tissue. Two published models of the distribution of blood within the layers of the skin were considered. One was described by Reuss and Siker[48] and later by Reuss,[49] and the other was described by Meglinski and Matcher.[50, 51]

Though they use different terminology, each model breaks the dermis down into four constituent layers: the papillary dermis, the papillary plexus, the reticular dermis, and the cutaneous plexus. Above these dermis layers is the epidermis (Meglinski and Matcher further

break this down into stratum corneum and living epidermis, but this work considered them as one layer), and below them is the hypodermis. A schematic of all of these layers is shown below in Figure 12.[49]

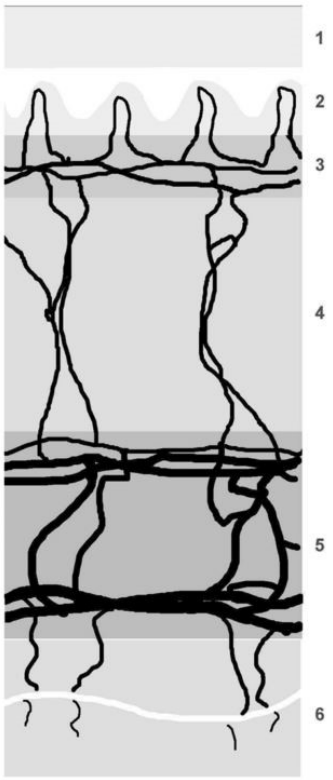

Figure 12. Schematic of the layers of the skin. 1: epidermis, 2: papillary dermis, 3: papillary plexus, 4: reticular dermis, 5: cutaneous plexus, 6: hypodermis. Reprinted from J. L. Reuss, "Multilayer modeling of reflectance pulse oximetry," *IEEE Transactions on Biomedical Engineering* **52**(2), 153-159 (2005) with permission from IEEE. © 2005 IEEE.

The epidermis, both the stratum corneum and the living portion, does not have any blood vessels and is instead served by the looping capillaries in the papillary dermis, which are the only blood vessels in the papillary dermis.[52] Gas exchange, delivery of nutrients, and removal of waste in the living epidermis are achieved entirely by diffusion between this layer and the capillaries of the papillary dermis. Each dermal papilla contains one capillary, which connects to the papillary

plexus.[53, 54] The arterioles of the papillary plexus, from which the papillary capillaries arise, range in diameter from 17 µm to 26 µm.[54] The arterioles in the cutaneous plexus have a diameter of approximately 50 µm.[55] Both the papillary dermis and the reticular dermis have relatively lower blood concentration than the papillary plexus and the cutaneous plexus, both of which are very rich in blood vessels. The thicknesses and blood concentrations of each skin layer in the anatomical models considered are given below in Table 6.[48-51] To make this work more specific to the wrist, where optical HR monitors for fitness tracking are typically placed, the thickness of the epidermis was adjusted from what was listed in the originally published models. Whitton and Everall measured the thickness of the epidermis on several body sites and found the epidermal thickness (mean ± standard deviation) of 39 samples from the wrist to be 80.7 µm ± 18.4 µm.[56] Thus, this work was performed assuming an epidermis thickness of 81 µm. Since the two anatomical models did not show agreement in their parameters, both were analyzed with Monte Carlo simulations.

Table 6. Thicknesses and blood concentrations of the layers of the skin.

Skin Layer	Thickness (µm)		Blood Concentration (%)	
	Anatomical Model 1[48, 49, 56]	**Anatomical Model 2[50, 51, 56]**	**Anatomical Model 1[48, 49]**	**Anatomical Model 2[50, 51]**
Epidermis	81	81	0	0
Papillary dermis	200	150	0	4
Papillary plexus	200	80	5.56	30
Reticular dermis	800	1500	4.17	4
Cutaneous plexus	600	80	20.37	10
Hypodermis	8000	6090	4.17	5

Though the pressure in the nailfold capillaries has been observed to be pulsatile[57, 58] and thus suggests that the pressure in the skin capillaries is, as well, these vessels do not contribute to the pulsatile component of a PPG signal. Capillaries are usually between 4 μm and 8 μm in diameter, with a length of 0.5 mm to 1 mm.[22] The radial distensibility of feline mesenteric capillaries has been measured to be 2.964 x 10^{-3} $mmHg^{-1}$ on average[59] and the radial compliance of porcine epicardial capillaries to be 8.5 x 10^{-3} μm/mmHg on average.[60] Since a capillary has an inner diameter that is approximately equal to the diameter of RBCs, any change in capillary cross-sectional area will not be enough to allow an accumulation of more RBCs per unit length. Thus, any volume pulse in the capillaries will yield a pulsatile plasma volume but not a pulsatile volume of the RBCs, where Hb resides, therefore eliminating the need to include this effect when modeling optical systems.

A wide range of flow rates can be found in the skin. Since a major function of the cutaneous circulation is thermoregulation, the mean blood flow in the skin is 20–30 times as large as the minimum value required for gas and nutrient exchange, and the maximum blood flow is 100–200 times as large as the minimum.[22, 61] With the assumption of a constant upstream pressure, the flow rate must change as a result of changes in the resistance of the cutaneous vasculature, which can be accomplished by changing the radius of vessels. In turn, a change in vessel radii implies a change in overall skin blood content. Since the resistance of an individual vessel is proportional to r^{-4}, the vessels can massively adjust the flow rate with small changes in caliber. The models presented in this section assume a typical cutaneous blood content, but deviations from the nominal values will affect the PPG signal.

Behzadi and Liu have presented a model of cerebral arteriolar compliance versus radius, with an example given for an arteriole of nominal radius 35 μm.[62] As stated previously, the range

of arteriolar diameters in the papillary plexus is approximately 17 μm – 26 μm (radius of 8.5 μm – 13 μm).[54] Though they have a thicker wall than arterioles found elsewhere in the body,[63] a first-order approximation was made that the radial compliance of these smaller arterioles is equal to that of the example, namely approximately 9.575 x 10^{-3} $mmHg^{-1}$.[62] Since the pulse pressure at the arteriolar side of the capillaries in the skin is 5 mmHg – 10 mmHg,[64, 65] the proportional volume change of the arterioles from diastole to systole was taken to be 0.15. Based on the total volume of the arterioles and smallest arteries, the capillaries, and the venules in canine mesentery,[22] the proportion of arteriolar volume relative to total vascular volume in the dermis was taken to be 0.39. The one exception was in the papillary dermis, since this layer's blood vessels are all capillaries (though the model described by Reuss and by Reuss and Siker does not include any blood in this layer to begin with).

Optical Properties of Epidermis, Bloodless Dermis, and Hypodermis

The epidermis has a blood content of zero *in vivo*, as its gas and nutrient exchange occurs via diffusion due to concentration gradients between the epidermis and the dermal papillary capillaries. Since this work involves the design of a dynamic phantom whose blood content in the dermis can change, though, the optical properties of the blood and those of the dermis itself needed to be separated. Due to the blood contained in the dermis, a human dermis sample must have its blood removed before characterization for this application. In the computational anatomical models, blood was modeled as 100% oxygenated for simplicity, due to the similarity between the spectra of oxygenated blood and deoxygenated blood in the 490 nm – 560 nm wavelength range. Due to the shallow penetration depth of green light in skin tissue, the hypodermis had little effect on the diffuse reflectance properties of the skin. Thus, it was considered as a simplified tissue with

a constant blood content inherent to the layer instead of a variable blood concentration added in separately to bloodless hypodermis.

In the epidermis, the main absorber is melanin. There are two main types of melanin found in the skin, eumelanin and pheomelanin, and within each category are many different specific molecules. When many different melanin molecules are combined, their individual absorption peaks blend together to form a flatter spectrum.[66] Keratins are the main scatterers in the epidermis, and collagen, which makes up anywhere from 18% to 30% of the dermis's volume, is the main scatterer in the dermis.[30, 67] In addition to these filamentous proteins, other structures in the skin that have a refractive index mismatch with their surrounding environment contribute to scattering, such as melanosomes in the epidermis's melanocytes, cell nuclei, plasma membranes, mitochondria, and other organelles.[30, 68]

Several works in the literature contain information about the optical properties of the epidermis, the dermis, and the hypodermis, a summary of which is below in Table 7, along with descriptions of the tissue preparation methods used. Differences between samples, different tissue preparation methods, and measurement error may all have contributed to the discrepancies between various data sets. Particularly when computing μ_a and μ_s' via IAD, the results are extremely dependent on the sample thickness, so any error in this measured value could have caused profound effects on the reported data. Similarly, a sample that does not have uniform thickness will introduce error, since solvers that compute optical properties generally assume a uniform thickness.

Additionally, as mentioned in CHAPTER III, the optical properties of *in vitro* samples are different than those of tissues *in vivo*.[30] Other important factors such as hydration and blood content can be quite different *in vitro* than they are *in vivo*. Furthermore, various tissue preparation

methods are described in Table 7, which means the tissues were likely affected differently and to varying degrees in their respective experiments. For example, heating a tissue can lead to protein denaturation. Bozec and Odlyha reported that hydrated collagen showed evidence of conformational changes, such as shrinking, at (58 ± 10) °C and evidence of the breaking of crosslinks at (65 ± 10) °C, though they also note that Miles and Bailey showed that the denaturation temperature of collagen depends on the heating rate.[69, 70] Several of the preparation methods described in Table 7 include temperatures near or at these values, and any structural changes due to denaturation will certainly affect the optical properties of the cutaneous tissue. For example, the scattering coefficient and scattering anisotropy depend on the size and shape of the scattering particles (often proteins), and the scattering coefficient also depends on the number density of scattering particles. All three of these protein parameters can be affected by tissue preparation and storage.

In addition to these sources of variability which affect the accuracy with which a particular sample is characterized relative to what was true *in vivo*, there are again the small measurement uncertainties that can lead to large error in computed output values. However, there is also inherent variability between samples due to parameters such as the number densities of melanin, keratin, and collagen, as well as the volume and number density of arterioles, capillaries, and venules within the tissue. These parameters cannot be realistically controlled for, so the values of optical properties listed in the literature must be taken as a general guideline that, with potentially large error, describes a subset of the possible values, rather than as measurements that have absolute authority.

Table 7. Tissue preparation methods and optical properties of epidermis, dermis, and hypodermis as found in the literature. Some values presented here were obtained from published plots and thus may have some error relative to the original data sets. Data with the number of samples or tissue preparation marked as "n/a" was calculated from a mathematical model. M–SD: mean minus standard deviation; M: mean; M+SD: mean plus standard deviation; RV: representative value. Some *g* values were not measured on the same samples that μ_a and μ_s' were measured on but were rather assumed based on previous work or added to the data sets later when reviews of the literature were published.

Tissue Type	**Tissue Preparation Method and Notes**	**Sample Size**	**λ (nm)**	**μ_a (cm^{-1})**	**μ_s' (cm^{-1})**	***g***
Epidermis[27, 71]	Skin excised from face, scalp, neck, and back; rinsed in PBS; epidermis cut with microcryotome to thickness of 60–100 µm; hydrated with saline; measured within 7 hours of excision.	7	525	5.562 (M)	63.35 (M)	0.8
Epidermis[72] (3.8% melanin)	n/a	n/a	525	22.47	42.95	Not given
Epidermis[72] (13.5% melanin)	n/a	n/a	525	78.42	42.95	Not given
Epidermis[72] (30.5% melanin)	n/a	n/a	525	176.5	42.95	Not given
Epidermis[27, 73]	Skin excised from upper leg, lower back, breast, thigh, abdomen, and groin; subcutaneous fat removed by scraping; dermis placed in contact with hot plate until epidermis was at 49 °C for 2 min; epidermis removed and placed over the surface of saline solution; measured within 1 hour of excision.	10	525	1.91 (M–SD) 5.764 (M) 9.546 (M+SD)	20.54 (M–SD) 27.55 (M) 34.64 (M+SD)	Not given

Table 7. Continued.

Tissue Type	Tissue Preparation Method and Notes	Sample Size	λ (nm)	μ_a (cm^{-1})	μ_s' (cm^{-1})	g
Fair-skinned Caucasian epidermis[27, 74, 75]	Skin obtained from abdomen and breast during autopsy and surgery; hypodermis scraped off; epidermis and dermis heated in 60 °C water for 30 seconds; epidermis teased off.	7	514	44 (RV)	139 (RV)	Not given
Epidermis[27, 76, 77]	Unknown. Note: These values considered multiple data sets.	Not given	517	19	102.2	0.787
Dermis[27, 78]	Sample collected from abdomen at autopsy; submerged in 55 °C water for 2 minutes; epidermis manually removed; dermis soaked in saline to remove residual blood; dermis cut with dermatome to thickness of 360 µm.	1	525	2.5838	87.1025	0.2411
Dermis[27, 71]	Skin excised from face, scalp, neck, and back; rinsed in PBS; dermis cut with microcryotome to thickness of 100–780 µm; hydrated with saline; measured within 7 hours of excision.	8	525	3 (M)	40 (M)	0.8

Table 7. Continued.

Tissue Type	Tissue Preparation Method and Notes	Sample Size	λ (nm)	μ_a (cm^{-1})	μ_s' (cm^{-1})	g
Dermis[27, 74, 79, 80]	Fresh abdominal skin taken at autopsy incubated at 37 °C for 12 hours in solution of 1% epidermolytic toxin and 20% fetal calf serum to remove stratum corneum; heated for 30 seconds in 60 °C water; epidermis teased off; dermis cut by dermatome into sections 100–300 µm thick. Note: μ_a and μ_s' values presented by Tuchin[27] were the spectral data published by Anderson et al.[79] scaled to the data at 633 nm published by Jacques et al.[80]	Not given	514	3	58	0.77
Dermis[27, 76, 77]	Unknown. Note: These values considered multiple data sets.	Not given	517	2.2	44.73	0.787
Hypodermis[27, 71]	Skin excised from face, scalp, neck, and back; rinsed in PBS; hypodermis cut with microcryotome to thickness of 280–800 µm; hydrated with saline; measured within 7 hours of excision.	10	520	4.4 (M)	33.1 (M)	0.8

In addition to these properties, the refractive index is approximately 1.45 for epidermis and 1.385 for dermis.[30] The refractive index for hypodermis was taken to be 1.41, a typical value for soft tissues. Three different sets of optical properties were chosen based on the aggregated data to model three different epidermis types: light epidermis, medium epidermis, and dark epidermis. Two models of bloodless dermis were used. Bloodless dermis model A was derived from the measurements performed by Prahl. This set of optical properties was used directly because the tissue preparation protocol mentioned a soaking step specifically to remove residual blood from the sample.[78] While the g value in this model was taken from the other dermis data sets because a value as low as 0.2411 strongly indicates experimental or mathematical error, the μ_s' value was still used in this modeling because it and g are derived from separate sets of measurements. μ_a and μ_s' were calculated for bloodless dermis model B by computing the mean from all four dermis data sets in Table 7. g for bloodless dermis model B was taken as the mean of the last two dermis g values in Table 7, since these were the most reliable values that were not designated as being assumed. The dermis samples that yielded the data in this table had absorption spectra that did not noticeably show the spectrum of HbO_2 in the 500 nm – 600 nm wavelength range and so were assumed to be mostly or completely bloodless.

Monte Carlo Simulations of Anatomical Models of the Skin and of a Model with Simplified Geometry

Monte Carlo modeling of the skin was performed for a wavelength of 525 nm, which is at the center of the range 490 nm – 560 nm. The optical properties shown below in Table 8 for each tissue type were used in Monte Carlo simulations and were the target values for the phantom materials. μ_a, μ_s, and g of each layer of the dermis were calculated from the bloodless dermis and blood parameters using (7), (11), and (17), respectively; bloodless dermis and blood were assumed

to compose 100% of the dermis volume. *n* was assumed to be a constant 1.385 for the entire dermis, regardless of blood content, since the values of *n* for dermis and blood are so similar and the volume fraction of blood is fairly low in most layers. In order to achieve adequate resolution in the fluence rate throughout the tissue, 10 million photon packets were launched in each simulation. To achieve adequate spatial resolution, the volumetric grid elements were defined to be concentric cylindrical shells with inner radii in multiples of 0.1 mm that were cut into sheets 1 μm thick.

Table 8. Optical properties used in Monte Carlo simulations of the anatomical skin models and as targets for phantom models. MC: Monte Carlo parameter; PM: phantom model target.

Tissue Type	**λ (nm)**	***n***	**μ_a (cm^{-1})**	**μ_s' (cm^{-1})**	***g***
Light epidermis	525	1.45	5.696	36.52	0.7785
Medium epidermis	525	1.45	28.49	39.74	0.7785
Dark epidermis	525	1.45	127.5	42.95	0.7785
Bloodless dermis model A	525	1.385	2.5838	87.1025	0.7785
Bloodless dermis model B	525	1.385	2.705	57.64	0.7785
Blood	525	1.385 (MC) 1.347 (PM)	165.48	18.42	0.9954
Hypodermis	525	1.41	4.4	33.1	0.8

Since the anatomical models described previously have large discrepancies between their parameters, both were simulated and evaluated, the results of which are shown and discussed below. Each simulation yielded an output of diffuse reflectance at the surface of the tissue as a function of the radial distance from the illumination. In order to combine all the data for each simulation into a single value, a specific geometry for an LED and a photodiode were used to calculate the total diffuse reflectance that would be captured under those conditions as an integral

over area. The geometry of the optics of the SVTronics AFE4403 Watch EVM was used for this calculation because that particular product allowed recording of raw optical signals *in vivo*, which could then be compared with the simulation results. Processing of the simulation outputs was performed with code written in MATLAB R2016b (The MathWorks, Inc., Natick, MA), which is included in Appendix A. A microscope image with 5x magnification of the optics in question is shown below in Figure 13, and the dimensions of the optical layout are shown in Figure 14.

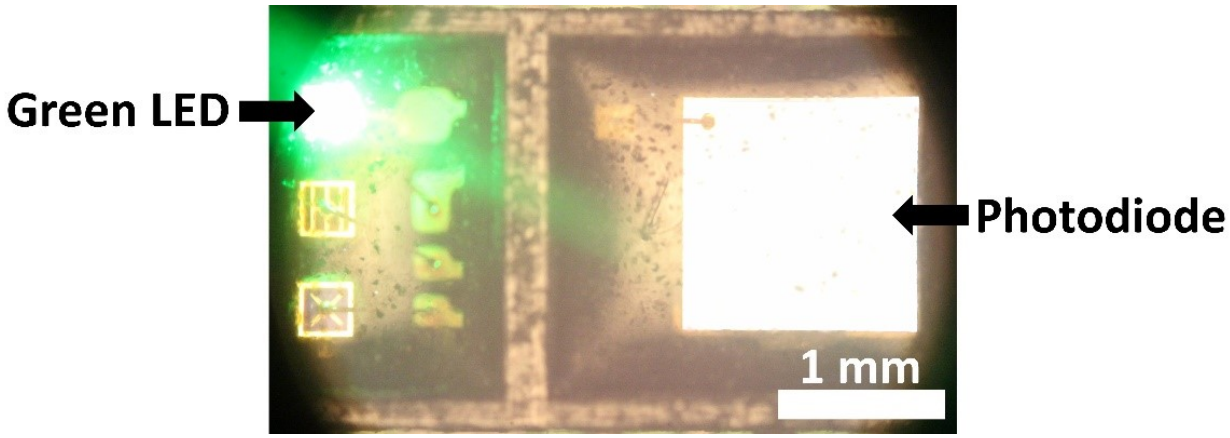

Figure 13. Optical components of the SVTronics AFE4403 Watch EVM under 5x magnification.

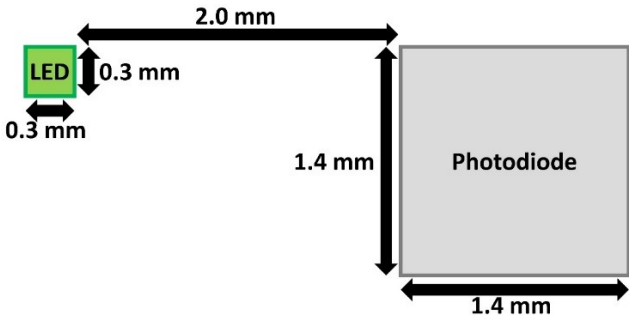

Figure 14. Geometry of the optical components of the SVTronics AFE4403 Watch EVM.

Each Monte Carlo simulation yielded a mean captured reflectance value, which was the mean of the captured weight of the individual photon packets. Monte Carlo simulations are a

stochastic method that inherently have error due to their random nature. This error can be minimized by simulating a large number of photon packets. In addition to minimizing the error of each individual simulation, multiple simulation runs can be performed to generate an output distribution. Each diastolic case and each systolic case were simulated eight times in order to obtain a mean of the mean and a standard deviation of the mean for each case. Simulating the reflectance in diastole $R_{diastole}$, which will also be called the baseline reflectance $R_{baseline}$, of the anatomical models laid out in Table 6 with the optical properties listed in Table 8 yielded the values shown below in Figure 15, which showed expected trends.

For each of the four combinations of anatomical and dermis models, the captured baseline reflectance decreased as the epidermis tone became darker. For each of the six combinations of epidermis and dermis models, anatomical model 1 had higher captured baseline reflectance than anatomical model 2. This was because it had a much lower blood concentration in the top 230 µm of the dermis, meaning the composite μ_a values given by (7) were also much lower. For each of the six combinations of epidermis and anatomical models, dermis model A had lower captured baseline reflectance than dermis model B because its μ_s value was much larger. This larger μ_s value meant that the simulated photon packets took a more tortuous path and thus had a longer path length within the absorbing dermis relative to the actual overall displacement than the photon packets in the dermis model A simulations did. This caused a higher overall probability of absorption, despite the similar absorption coefficients for the bloodless dermis models and, thus, for the dermis models with blood included.

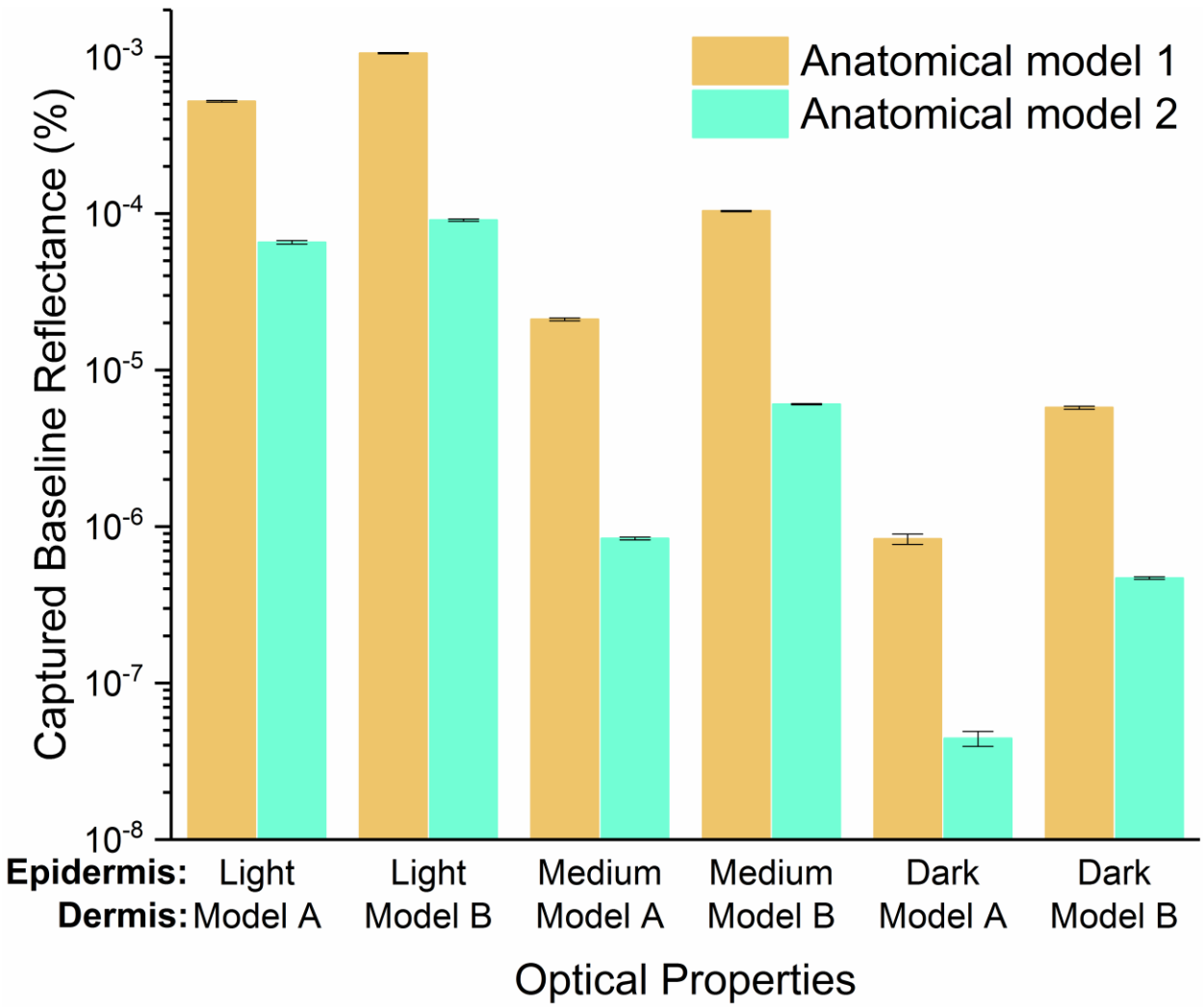

Figure 15. Simulated baseline reflectance in diastole captured by the photodiode with the optical layout of the SVTronics AFE4403 Watch EVM. Each bloodless dermis model was used in combination with each epidermis tone.

The optical properties used in simulating the reflectance in systole ($R_{systole}$) captured by the photodiode were calculated in the same manner as when simulating $R_{diastole}$, except the concentration of blood in each layer was adjusted to account for the pressure pulse. As mentioned previously, the arteriolar volume of each dermis layer was taken to be 39% of the total microvasculature volume, and the cross-sectional area of the arterioles was taken to increase by 15% from diastole to systole. The one exception to this was in the papillary dermis, where the

arteriolar volume is 0% of the microvasculature volume. Thus, the concentration of blood in each dermis layer *i* other than the papillary dermis was calculated as follows.

$$C_{blood,systole,i} = 0.61C_{blood,diastole,i} + 1.15 \cdot 0.39C_{blood,diastole,i} = 1.0585C_{blood,diastole,i} \tag{27}$$

The pulsatile reflectance $R_{pulsatile}$, given in (28), which is the optical signal the sensor must be able to resolve in magnitude in order to detect a periodic HR signal, was extremely small, as shown in Figure 16.

$$R_{pulsatile} = R_{diastolic} - R_{systolic} \tag{28}$$

While the absolute values are much smaller, the mean pulsatile reflectance values showed the same trends as those described for the captured baseline reflectance above. $R_{systole}$ is typically less than $R_{diastole}$ due to the increased local volume of blood causing more absorption. However, the error bars for two combinations of parameters reach into the negative values, which cannot be adequately represented on a logarithmic scale. The results of unpaired two-sample, two-tailed Welch's *t*-tests between the distributions of $R_{diastolic}$ and $R_{systolic}$ for each set of parameters are also shown in Figure 16, with a statistically significant difference observed for all but one set.

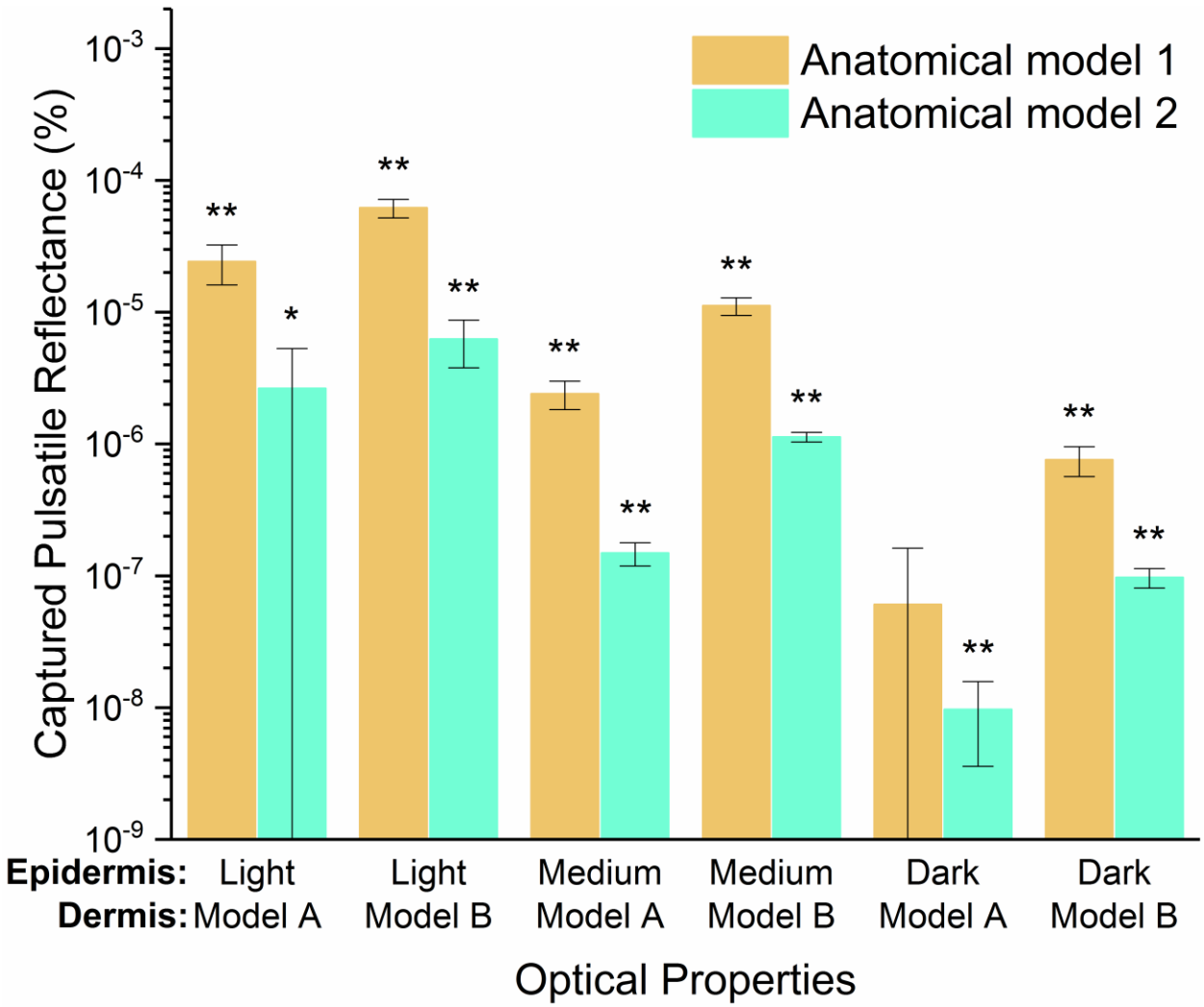

Figure 16. Simulated pulsatile reflectance captured by the photodiode with the optical layout of the SVTronics AFE4403 Watch EVM. Each bloodless dermis model was used in combination with each epidermis tone for each of the related simulations. *$R_{diastole}$ and $R_{systole}$ statistically significantly different for α=0.05. **$R_{diastole}$ and $R_{systole}$ statistically significantly different for α=0.01.

The maximum pulsatile reflectance from these simulations was ~6.2x10^{-5}%. This means that for an illumination of 2 mW, the pulsatile optical power detected would be ~1.24 nW. The resolution of many photodiodes is in the nW range, with some going as low as 10 pW. In this case, a strong illumination power, light epidermis tone, and very clean captured signal would still be required in order to yield a HR reading. However, even under these ideal signal generation

conditions, it is unlikely that the photodiodes in optical HR monitors designed for fitness applications have photodiodes that are sensitive enough for this task. However, the fact that they are able to give a HR output means that they are capturing a pulsatile signal that is sufficiently large to be well-resolved in amplitude. This suggests that neither of the anatomical models adequately describes the generation of a PPG signal at the wrist with 525 nm light.

The signal-to-baseline ratio (SBR) was calculated for each anatomical model with each epidermis tone, as in (29). In real circuitry, for a constant baseline value, a high SBR means that the captured signal can be amplified in the first electronic stage without first being conditioned by a highpass filter. A low SBR means that in order to prevent clipping of the amplified signal due to finite output range without sacrificing gain, the captured signal must go through a highpass filter to eliminate the zero-frequency and weaken the low-frequency content. However, the later the amplification stage is, the lower the output signal-to-noise ratio (SNR) will be.

$$SBR = 100\% \left(\frac{R_{diastole} - R_{systole}}{R_{diastole}} \right) \tag{29}$$

Each anatomical model tended to have a SBR that increased as the epidermis tone was changed from light to medium and from medium to dark. The exception to this was the model with anatomical model 1, dermis model A, and dark epidermis. In addition to being the only model whose SBR broke this trend, it was the only one whose SBR error bars reached below 0%. This is logically consistent with the fact that it was the only model whose $R_{diastolic}$ and $R_{systolic}$ values were not statistically significantly different from each other.

However, the SBR is a misleading metric if the baseline value is not kept in mind. Though the SBR is increasing with darker epidermis, this value is calculated by taking the ratio of two extremely small numbers. Thus, it is important to note that these increasing SBR values come at

the expense of the pulsatile signal becoming prohibitively small due to the noise present in real signals and the resolution limitations of optical detectors and of electronics.

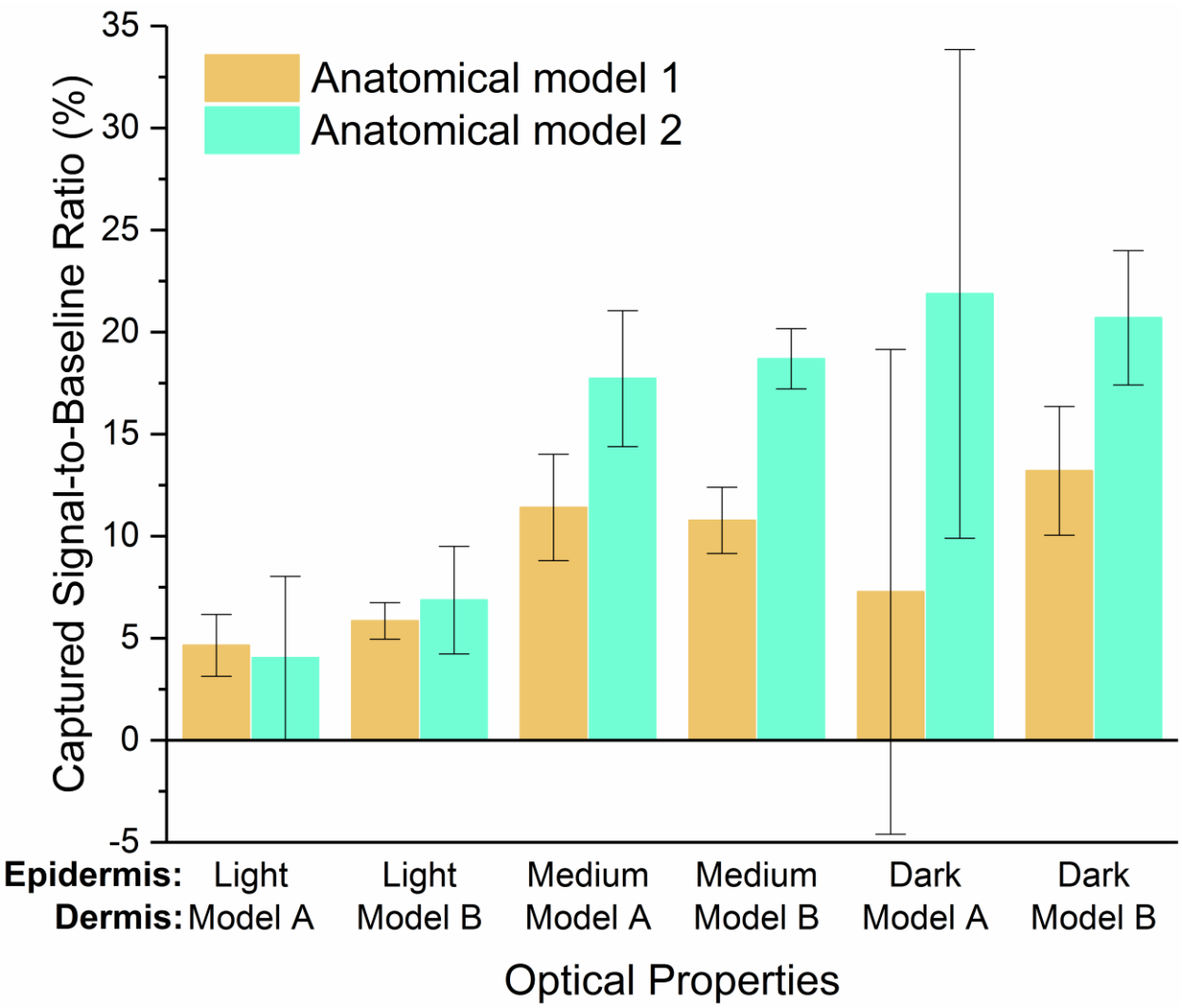

Figure 17. Simulated signal-to-baseline ratio captured by the photodiode with the optical layout of the SVTronics AFE4403 Watch EVM. Each bloodless dermis model was used in combination with each epidermis tone for each of the related simulations.

Comparison of Simulation Results of Anatomical Models of the Skin to *In Vivo* Data

In order to check the results of these simulations, *in vivo* data was collected in the laboratory with the SVTronics AFE4403 Watch EVM, using green illumination, as part of the

same IRB-approved protocol mentioned previously. Data was collected on one individual with light epidermis and one individual with medium epidermis, though here, these designations are subjective and may or may not coincide with the epidermis models used in the Monte Carlo simulations. The skin of each individual while wearing the device is shown in Figure 18 below.

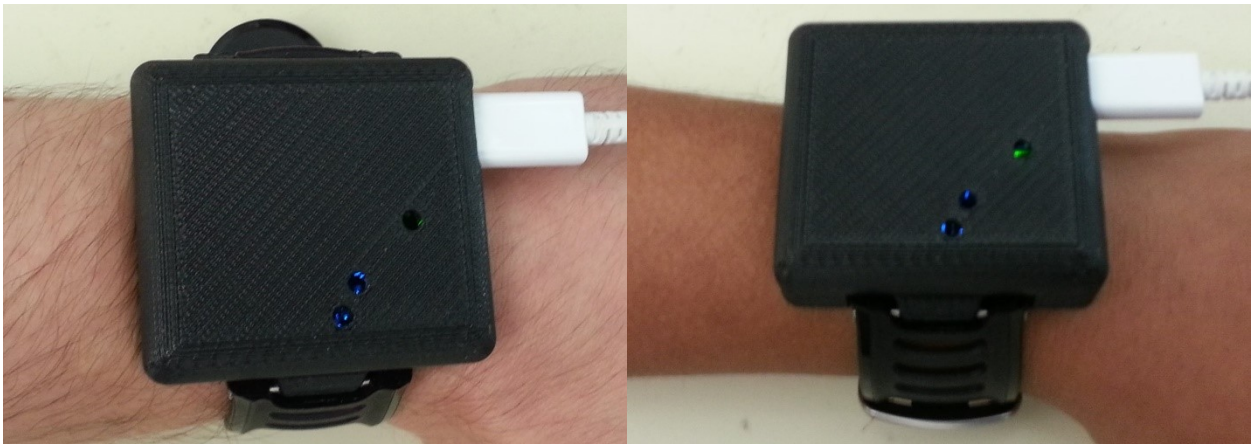

(a.) (b.)

Figure 18. Skin tones of human subjects who wore the SVTronics AFE4403 Watch EVM for *in vivo* PPG collection with green illumination. (a.) Light epidermis. (b.) Medium epidermis.

The AFE4403 integrated circuit (Texas Instruments Incorporated, Dallas, TX) that is contained within the SVTronics AFE4403 Watch EVM had the option to implement an ambient cancellation current for the purpose of canceling out signal due to ambient light before digitization occurred; this cancellation current feature was not used. Instead, the signal analyzed had the ambient signal removed after digitization by subtracting the ambient signal collected with the LED off from the signal collected with the LED on. To further minimize the effect of ambient light, this data collection was performed in a dark room.

Six data sets were collected from each subject. The subjects sat in a chair with their legs uncrossed and rested their left forearm on a table at approximately stomach or chest height. Wearing the monitor on their left wrist with the optical components on the posterior side, the

subjects sat still for ~2–3 minutes to allow the blood content in their wrist to stabilize. Then, data was collected for one minute. In between collection of successive data sets, the subjects removed the monitor from their wrist and were allowed to move. This was allowed in order to promote independence between trials, both by allowing the cutaneous blood content in the wrist to be modulated through positional changes and by ensuring the monitor would be strapped on in a slightly different location and possibly with a different tightness.

Each data set was processed to determine its baseline value and its pulsatile value. The data was passed through a second-order zero-phase digital highpass Butterworth filter with a cutoff frequency of 0.15 Hz to remove zero-frequency and weaken low-frequency content to aid in accurate feature detection. A second-order zero-phase digital lowpass Butterworth filter with a cutoff frequency of 25 Hz was subsequently applied to decrease the high-frequency noise content. Then, for each pulse, the maximum reflectance $R_{diastole,i}$ and the minimum reflectance $R_{systole,i}$ of each pulse were identified, where i refers to a specific PPG pulsation. The baseline reflectance and pulsatile reflectance for each data set were taken as in (30) and (31), respectively.

$$R_{baseline} = \frac{1}{k}\sum_{i=1}^{k} R_{diastole,i} \tag{30}$$

$$R_{pulsatile} = \frac{1}{k}\left(\sum_{i=1}^{k} R_{diastole,i} + \sum_{i=1}^{k} R_{systole,i}\right) \tag{31}$$

Then, the mean and standard deviation of $R_{baseline}$, of $R_{pulsatile}$, and of the SBR were calculated for the light epidermis case and the medium epidermis case, as shown in Figure 19. There were large discrepancies between the *in vivo* data and the simulation results.

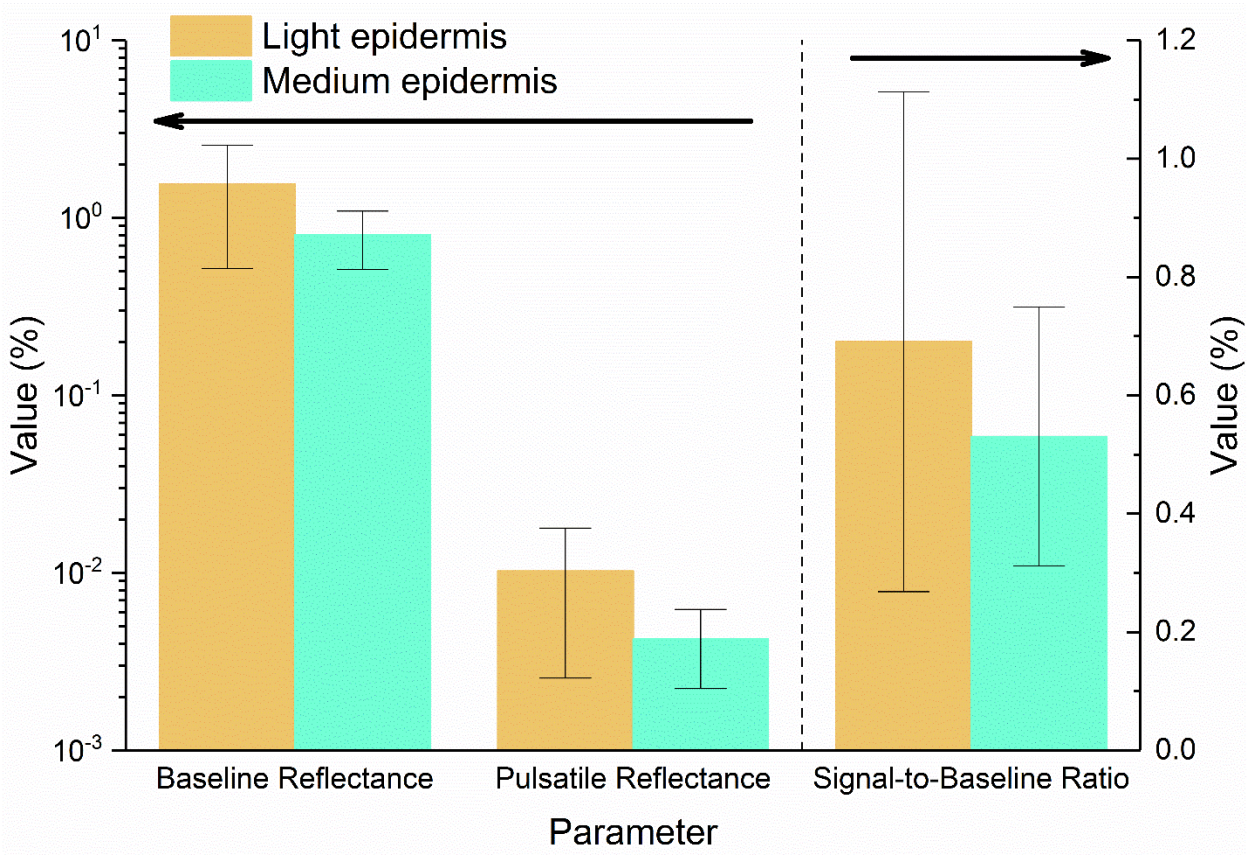

Figure 19. *In vivo* captured baseline reflectance, captured pulsatile reflectance, and signal-to-baseline ratio of light epidermis and medium epidermis. Baseline and pulsatile reflectance are shown on the left y-axis (logarithmic scale), and signal-to-baseline ratio is shown on the right y-axis (linear scale).

The raw *in vivo* optical data was converted to a voltage by the watch, so a calibration curve was created that indicated that 1 mV at the output corresponded to 0.184 µW of optical power captured by the photodiode. Since the illumination power was measured to be 891 µW, this means 1 mV at the output corresponded to 2.07 x 10^{-2}% reflectance. The mean baseline reflectance and the mean pulsatile reflectance *in vivo* were over three orders of magnitude and two orders of magnitude larger, respectively, than the closest corresponding mean value predicted by the models used in the Monte Carlo simulations, both for light epidermis and medium epidermis. The increased baseline signal *in vivo* can be at least partially explained due to the nature of the

illumination. The Monte Carlo modeling simulates an infinitely narrow collimated illumination beam that is orthogonal to the surface of the tissue, meaning all specularly reflected light will undergo no lateral displacement from the illumination beam. In the laboratory with an LED illumination, however, there is a finite divergence angle that allows some specularly reflected light to strike the photodiode. However, the strength of this effect was not quantified in this work.

The difference between the magnitude of the pulsatile component of the simulated signal and that of the measured *in vivo* signal cannot be explained by the same phenomenon. The *in vivo* data showed a mean pulsatile reflectance of approximately 1.0×10^{-2}% for light epidermis and 4.2×10^{-3}% for medium epidermis, which correspond to an optical power of 91 μW and 38 μW of captured optical power, respectively. This is two to three orders of magnitude larger than the closest corresponding mean value predicted by the Monte Carlo simulations for each epidermis. The larger *in vivo* pulsatile amplitude corroborates the idea that was based on typical photodiode specifications that the models used in the Monte Carlo simulations did not yield results indicative of what truly happens in the wrist. Though there were undoubtedly some differences between the optical properties of the epidermis used for the simulations and those found in the *in vivo* case, those are not enough to explain several orders of magnitude difference for multiple output parameters.

In order to rule out the possibility that this low simulated captured optical power was because the blood content was too high, simulations were performed with an epidermis thickness of 81 μm, a single dermis layer 1.8 mm thick with a zero blood content, and a hypodermis thickness of 8 mm. Each case, consisting of a particular epidermis model and bloodless dermis model, was simulated eight times with 10 million photon packets launched per simulation. These results are shown as the mean ± standard deviation per simulation below in Figure 20.

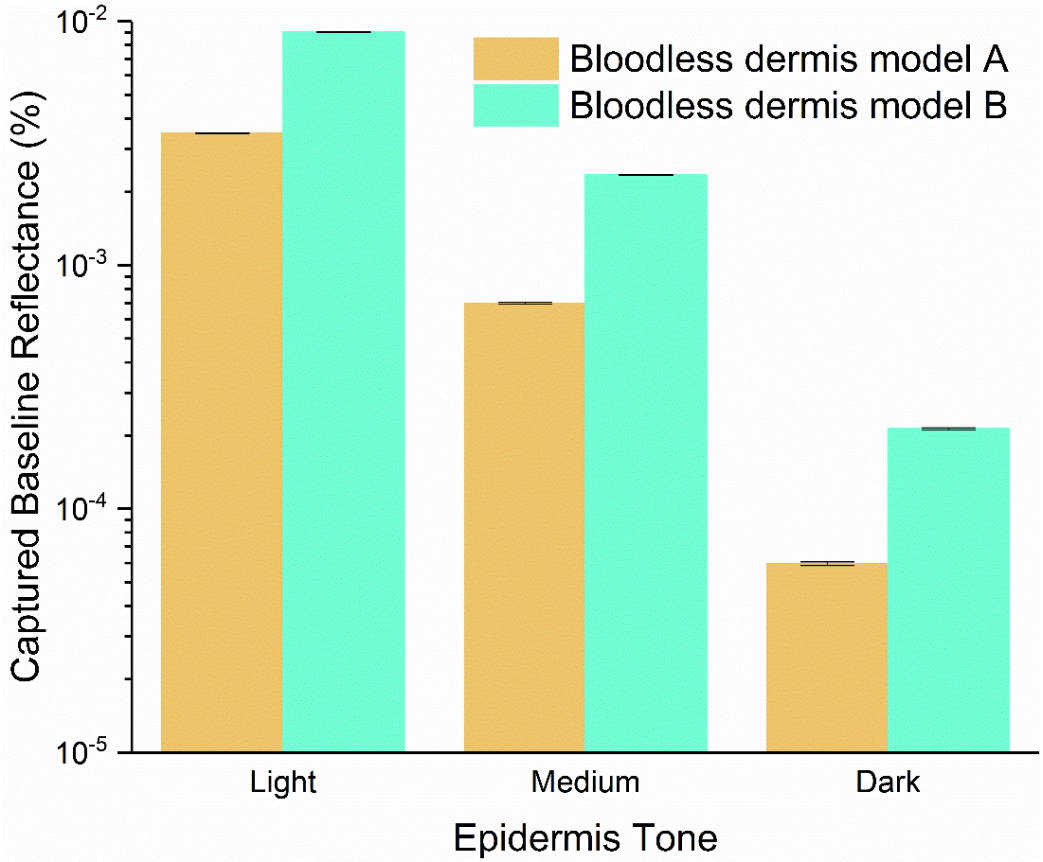

Figure 20. Simulated baseline reflectance captured by SVTronics AFE4403 Watch EVM for skin with no blood in the dermis.

The captured baseline reflectance values for the case of bloodless dermis range from about 6.7–100 times, 23–800 times, and 37–1350 times as large as with blood included for light, medium, and dark epidermis, respectively. However, even the simulations with light or medium epidermis and bloodless dermis for dermis model A or B show a baseline reflectance smaller than the pulsatile amplitudes that were measured *in vivo*. Thus, possible overestimates of the cutaneous blood content are not sufficient to explain the discrepancy between the Monte Carlo simulations and the *in vivo* data.

However, before the next round of simulations was performed, the best out of the four models was chosen. This choice was made by comparing the relationship between simulated skin

with light epidermis to that of simulated skin with medium epidermis with the relationship between *in vivo* skin with light epidermis and *in vivo* skin with medium epidermis. These relationships were examined by calculating the ratios of light epidermis output values to medium epidermis output values.

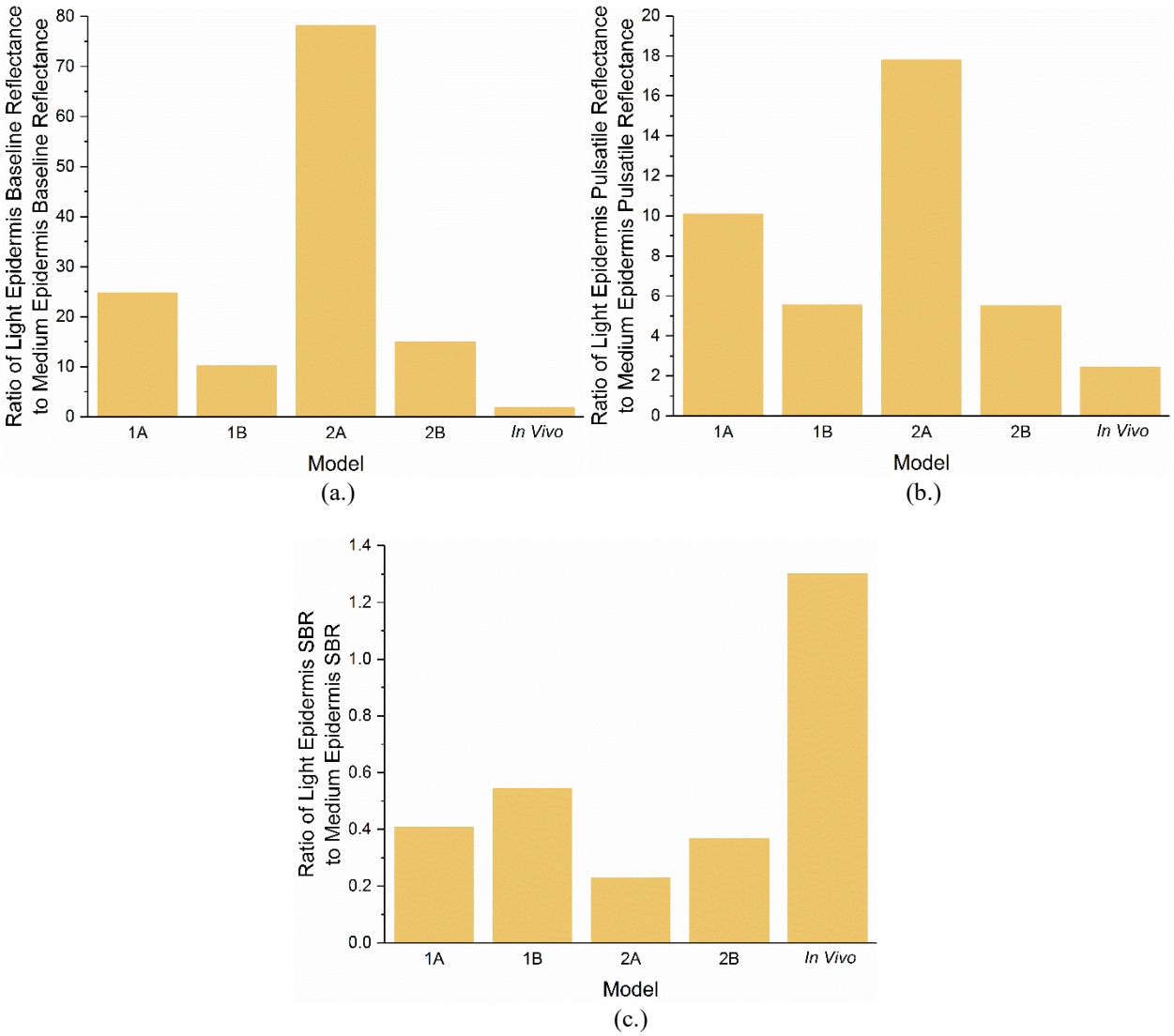

Figure 21. Comparison of the four simulated models with *in vivo* data. The ratios of the light epidermis values to the medium epidermis values are shown for (a.) baseline reflectance, (b.) pulsatile reflectance, and (c.) signal-to-baseline ratio.

While the *in vivo* data in Figure 21 does not match any of the simulated models particularly well, anatomical model 1 with dermis model B is the closest representation. Namely, it is has the closest light-to-medium ratio value for baseline reflectance and SBR. While anatomical model 2 with dermis model B is slightly better matched for the pulsatile reflectance than model 1B, these two values differ by less than 0.5%. Thus, model 1B was considered to be the best of the four models overall.

It has been suggested in the literature that the traditional belief that the pulsatile signal component of a PPG is due to local changes in blood volume is not accurate in the case of green illumination and that it may be due to perturbations of the tissue's absorption and scattering coefficients as a result of tissue compression due to the blood pressure pulse.[81-83] Though the optical properties of skin tissue have been shown to be pressure-dependent,[41] this explanation appears improbable, particularly without any specific data describing the pressure values achieved in the tissue and the corresponding optical properties as a function of that pressure.

Monte Carlo Simulations of Models of the Skin with Simplified Geometry

While the simulated models do not accurately describe the PPG signal, it is still worthwhile to determine if a complex multilayered tissue structure can be modeled with a simplified topology to generate a comparable dynamic diffuse reflectance as a function of radial distance from the illumination.

Due to the difficulty of creating a liquid phantom with the scattering properties of whole blood, the effect of which is small compared to that of bloodless dermis, the blood phantom was modeled computationally as a purely absorbing medium with the same μ_a value as in the anatomical models in order to match what was practical to develop in the laboratory. Additionally, the solid phantoms were made with PDMS, and one of the incorporated optical agents was Al_2O_3

microspheres with a median diameter in the range of 0.5 μm – 1 μm. As shown in the following chapter, Mie theory predicts a scattering anisotropy of $g \approx 0.8858$ for such particles dispersed in PDMS. Thus, PDMS phantom materials were represented in the Monte Carlo simulations as having this g value, while keeping the same μ_a and μ_s' values as in the simulations of the anatomical models. Due to the refractive indices of PDMS and of deionized water (DI H_2O) being slightly different from the values for actual tissue, the Monte Carlo simulations of the model with simplified geometry meant to emulate phantoms to be fabricated in the lab utilized the optical properties shown below in Table 9.

Table 9. Optical properties used in Monte Carlo simulations of the skin model with simplified geometry.

Tissue Type	**λ (nm)**	**n**	**μ_a (cm^{-1})**	**μ_s' (cm^{-1})**	**g**
Light epidermis	525	1.41	5.696	36.52	0.8858
Medium epidermis	525	1.41	28.49	94.72	0.8858
Dark epidermis	525	1.41	127.5	42.95	0.8858
Bloodless dermis	525	1.41	2.705	57.64	0.8858
Blood	525	1.33	165.48	0	0

The simplified models that were simulated have a geometry as shown below in Figure 22. The simplified models consisted of an epidermis phantom layer, two phantom layers of bloodless dermis model B, and a blood phantom layer. (There was alternatively only one phantom layer of bloodless dermis if the depth of the blood phantom layer was zero.) The epidermis layer had a thickness of 81 μm, and the dermis and blood layers had a combined thickness of 1.8 mm. These thicknesses correspond to those from the anatomical models. Sweeps were performed of the blood layer's thickness and of its depth beneath the surface of the bloodless dermis in order to determine

what geometries would yield a captured reflectance similar to what the anatomical models gave. Since the full tissue phantom being simulated was only 1.881 mm thick without the inclusion of the hypodermis, there was some optical power that transmitted all the way through the model and out the bottom. The maximum transmittance though the bottom surface for any combination of blood layer depths and thicknesses was 0.97%, 0.68%, and 0.25% for light epidermis, medium epidermis, and dark epidermis, respectively. Since the dermis material was simulated with a refractive index of 1.41 and the tissue edges were in contact with a medium with $n = 1$, the amount of power reaching the entire bottom surface of the model was calculated to a first approximation as being ≤1.0% in all cases. This was based on the admittedly inaccurate assumption that all light reaching this interface is traveling perpendicular to the interface, but it was only necessary to know on what order the value was. This allowed for the conclusions that any reflected energy traversing all the way back to the illuminated surface of the model and then exiting the tissue in the specific geometrical range where the photodiode is situated was negligible in these Monte Carlo simulations and that any light lost by transmission through the bottom surface was also negligible. The results of these simulations are shown in Figure 23, Figure 24, and Figure 25.

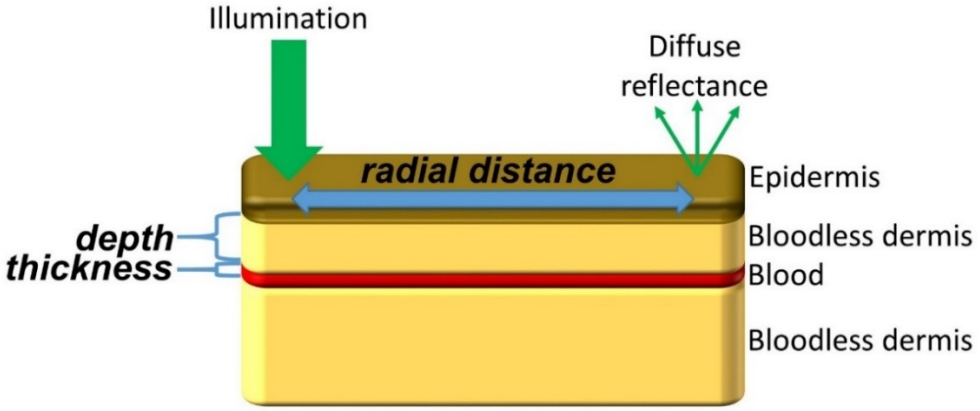

Figure 22. Skin model with simplified geometry.

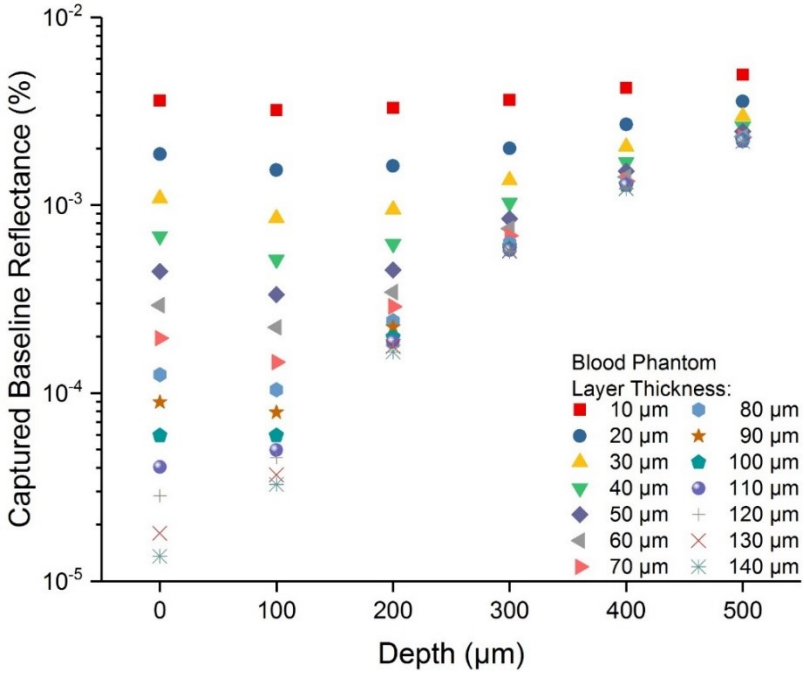

Figure 23. Simulated baseline reflectance captured with optical properties corresponding to those of a skin phantom with light epidermis and simplified layered geometry. The geometry of the optical components was defined by the SVTronics AFE4403 Watch EVM.

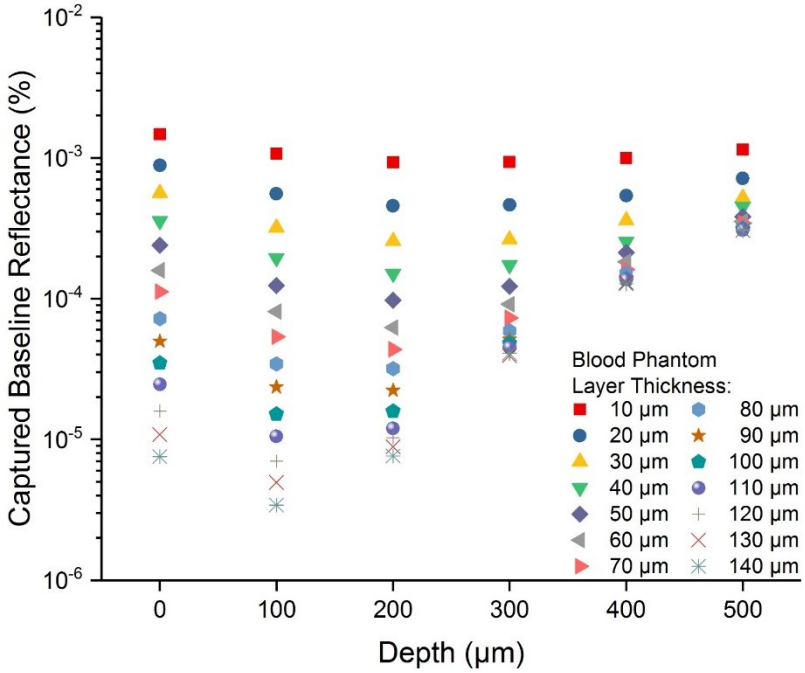

Figure 24. Simulated baseline reflectance captured with optical properties corresponding to those of a skin phantom with medium epidermis and simplified layered geometry. The geometry of the optical components was defined by the SVTronics AFE4403 Watch EVM.

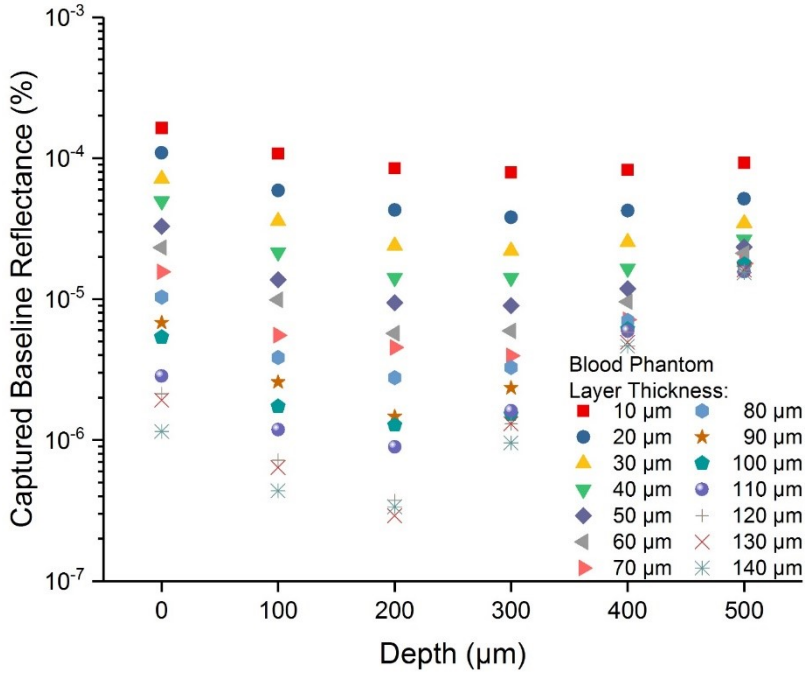

Figure 25. Simulated baseline reflectance captured with optical properties corresponding to those of a skin phantom with dark epidermis and simplified layered geometry. The geometry of the optical components was defined by the SVTronics AFE4403 Watch EVM.

As expected, the captured baseline reflectance decreased as the thickness of the blood phantom layer increased, causing more absorption. However, the captured baseline reflectance showed quite a reduced dependence on blood phantom layer thickness for deeper blood layers when compared to shallower blood layers. This was because the deeper the blood was, the higher the percentage of light that was interacting only with the thick bloodless dermis layer and never reaching the blood layer.

In addition, as the blood phantom layer moved away from the bottom of the epidermis and a thickening bloodless dermis layer was introduced, the captured baseline reflectance had a relative minimum at a nonzero depth in many cases. This was likely because of two competing phenomena. First, as the blood layer moved deeper, more optical power was able to reach the photodetector without ever interacting with the blood layer. This meant the blood absorbed less power overall.

Second, however, as opposed to the anatomical models, which were simulated with a constant refractive index throughout the entire dermis, the models with simplified geometry were simulated with a bloodless dermis phantom and a blood phantom of different *n* values. This meant that specular reflections occurred within the dermis. Thus, less power reaching the blood layer also caused less absolute power to be specularly reflected off the interface between the top bloodless dermis layer and the blood layer.

Since the simplified model utilized bloodless dermis model B, its simulation results were compared to the results with bloodless dermis model B in Figure 15. Each simplified model had several combinations of depths and thicknesses that allowed it to match the captured baseline reflectance of the anatomical models. Because of this, anatomical considerations led to narrowing down the choices to a depth of 300 µm. This was because this depth below the surface of the dermis is either in or near the papillary plexus, depending on which anatomical model is followed, which is the shallowest layer with a pulsatile volume. Thus, this made the most sense as a representation of the dermal blood for light that has a shallow penetration depth. The thickness of the blood layer necessary to match the captured baseline reflectance in the anatomical model simulations increased with darkening epidermis tone, with the best model out of those investigated being that with a blood phantom layer thickness of approximately 40–50 µm, 50–60 µm, and 60–70 µm for light, medium, and dark epidermis, respectively. The SBR in Figure 17 can be used to estimate the change in blood layer thickness necessary to move from a representation of diastole to a representation of systole and to thus yield the appropriate dynamic phantom geometry.

The simplified models with a blood phantom layer depth of 300 µm and thickness ranging from 40 µm to 60 µm are shown in relation to anatomical model 1 with bloodless dermis B below in Figure 26. From this data, a single thickness of 55 µm can be estimated to be an adequate model

for skin with each epidermis tone that was considered. The discrepancies in the values that would be yielded by this 55-µm thickness when compared to anatomical model 1 with dermis model B are acceptable because of the heavy dependence of its captured baseline reflectance on its absorption coefficients, scattering coefficients, and layer thicknesses. This is shown in Figure 27 below, which describes the change in captured baseline reflectance as μ_a, μ_s (but not g), and layer thickness were varied ±10%, one parameter at a time in one layer at a time, with all other values held constant at their original values. The dependence is shown to be quite strong for the epidermis and papillary dermis in the case of light epidermis, along with μ_a in the papillary plexus. For medium epidermis, a similar result is observed, along with an increased dependence on μ_a in the reticular dermis. For dark epidermis, changed parameters in any of the top four layers, along with the thicknesses in the cutaneous plexus and hypodermis, are shown to have a sizeable effect on the captured baseline reflectance. Furthermore, *in vivo* cases would likely have deviations from the anatomical models in multiple parameters simultaneously. Such deviations could yield changes in the baseline in either the opposite or the same direction, leading to smaller or even larger total changes.

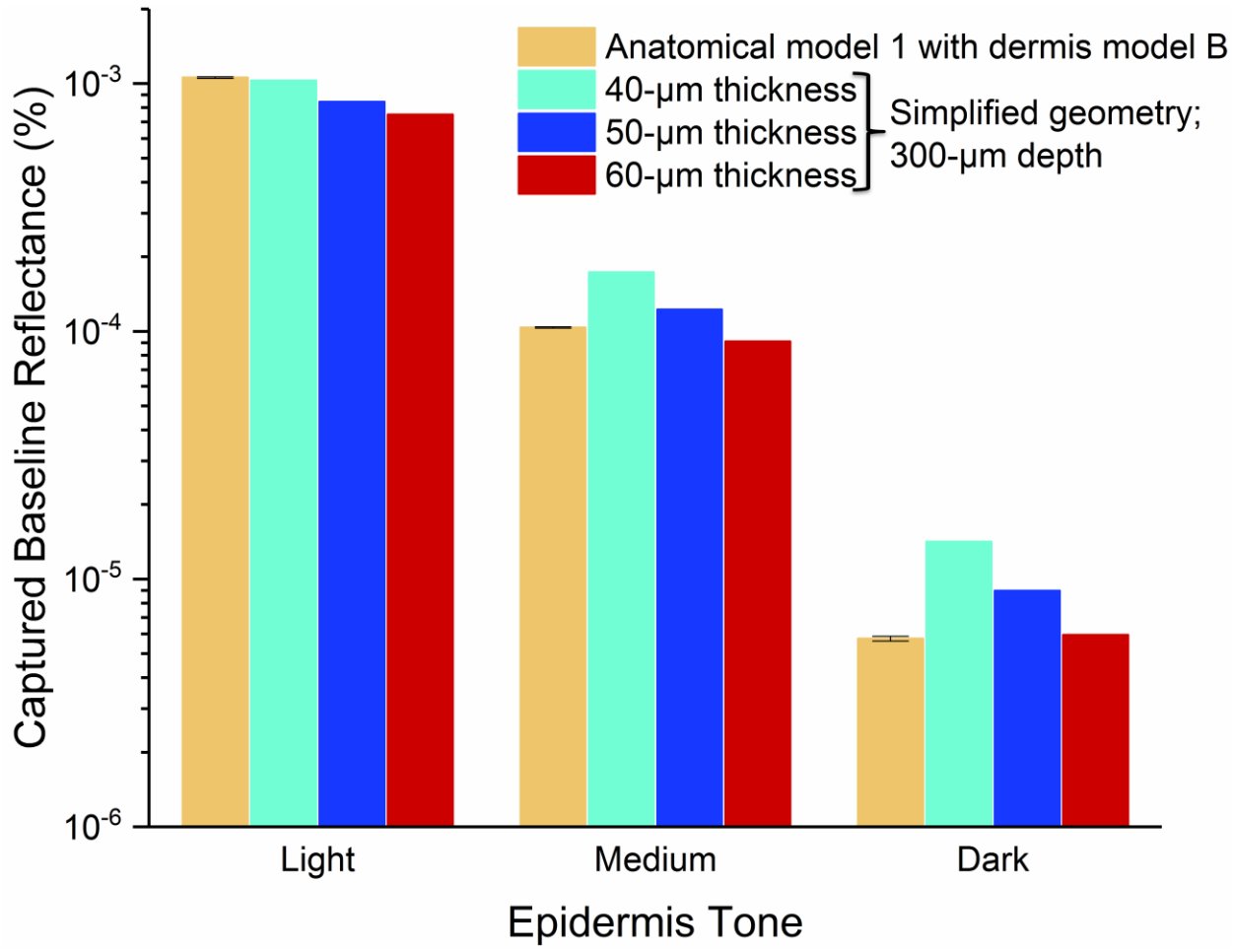

Figure 26. Simulated captured baseline reflectance from selected phantom models compared to that of anatomical model 1 with dermis model B.

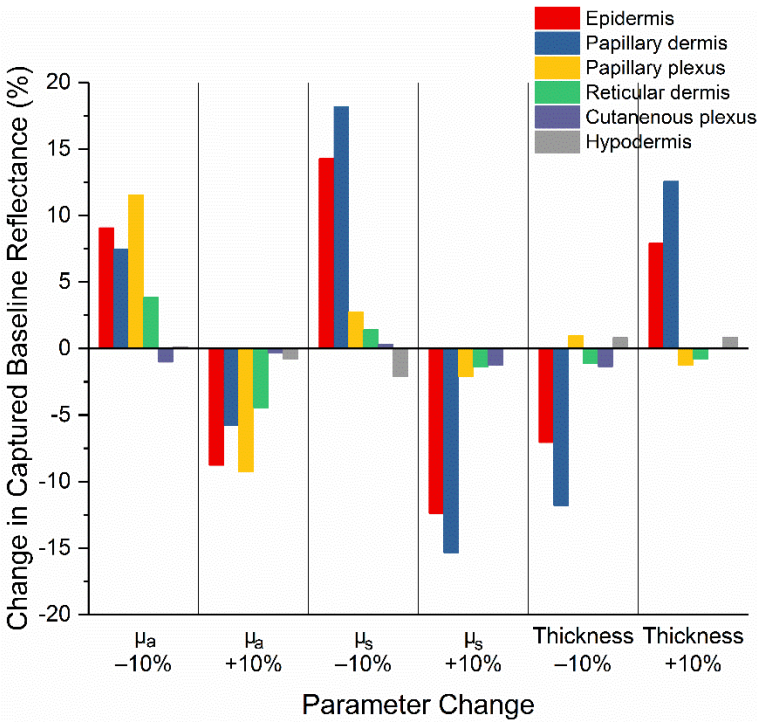

(a.)

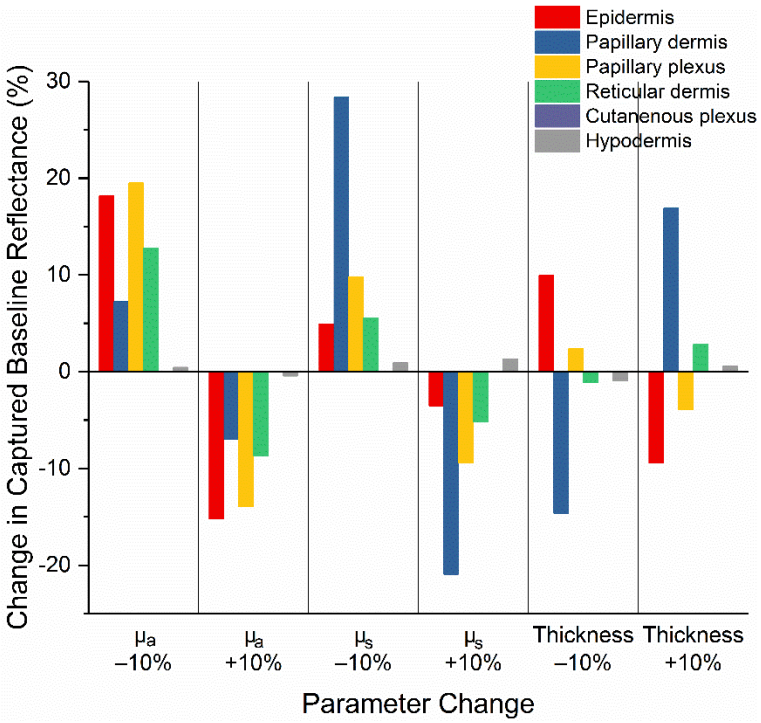

(b.)

Figure 27. Change in simulated captured baseline reflectance for anatomical model 1 with bloodless dermis model B due to change in various parameters in each layer. (a.) Light epidermis. (b.) Medium epidermis. (c.) Dark epidermis.

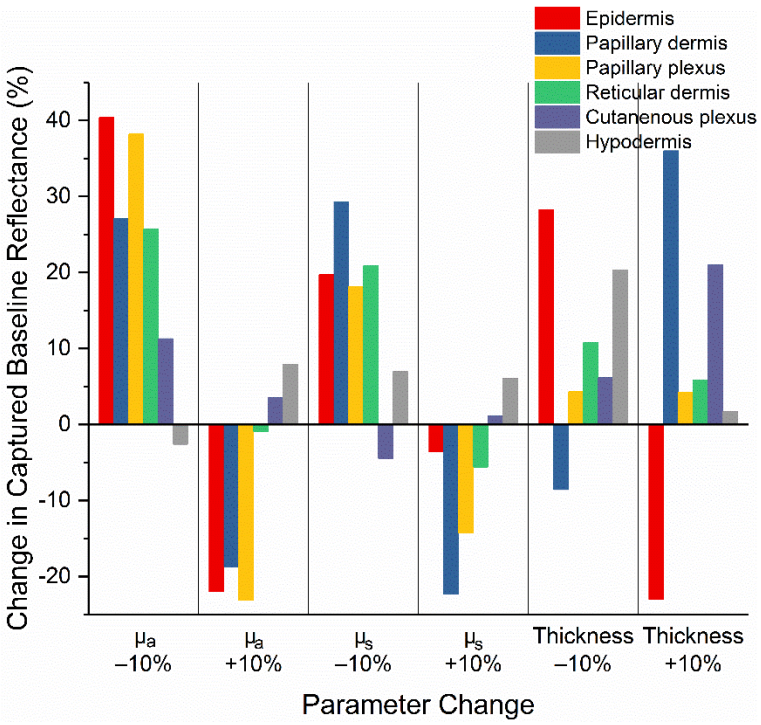

(c.)

Figure 27. Continued.

Development of Epidermis Phantoms and Bloodless Dermis Phantom

The epidermis and dermis phantom materials were made with a similar procedure as was used for the single-vessel skin phantoms. As explained earlier, the reflectance captured as a result of a lack of hypodermis was negligible, so no hypodermis phantom material was developed. This time, the optical agents were added to the Sylgard 184 curing agent, which is much less viscous than the Sylgard 184 base. Evenly incorporating the optical agents in the curing agent was thus a much easier and faster process than in the base. The mixture either was stirred manually and sonicated or was stirred with a magnetic stir bar on a stir plate at maximum speed. Then, the base was added and mixed in manually. Since the optical agents started off only in the curing agent and the clear base was added later, visual homogeneity indicated that the base and the curing agent

were well-mixed and would thus crosslink properly. Only thin slabs of each formulation were made, which were used for the purpose of optical characterization.

One of two sets of optical agents was used in each potential phantom material. The first set was MF42 and Al_2O_3 particles, as used by Lualdi et al.[42] and in the light single-vessel skin phantom described previously. As before, the Al_2O_3 particles had a median diameter in the range of 0.5 µm – 1 µm. The set of optical agents used in the remaining potential phantom materials was a combination of India ink (Higgins, Leeds, MA) and Al_2O_3 particles with 0.5 µm – 1 µm median diameter. This combination had the advantage of one being a pure absorber and the other being a pure scatterer, which allowed easier tuning of optical properties. However, for any work that involves multiple wavelengths of light, it may be difficult to tune a single phantom for each wavelength simultaneously using India ink. This obstacle can be overcome simply by using narrowband absorbers that have absorption peaks near the wavelengths of interest, as opposed to a single broadband absorber.

The problems encountered when characterizing the single-vessel skin phantom formulations were resolved here. Thinner samples were used, typically less than 600 µm thick. Additionally, each sample's reflectance was compared only to that of a single reflectance standard. If the reflectance of the sample was less than 10%, the 10% reflectance standard measurement was used as a reference. If the reflectance of the sample was greater than 10% but less than 50%, then the 50% reflectance standard measurement acted as a reference. If the reflectance of the sample was greater than 50%, then the illumination measurement with a capped exit port was approximated as a 100% reflectance reference.

Again, g could not be calculated for formulations containing MF42 due to its unknown composition. However, formulations with India ink instead of MF42 could be described

mathematically, under the assumption that the Al_2O_3 particles were spherical. The scattering anisotropy as a function of the diameter of Al_2O_3 particles dispersed in PDMS was calculated using (19)–(25) for the phantoms with India ink instead of MF42 and is shown in Figure 28. The mean of the *g* values at 525 nm for the diameters shown was 0.8858.

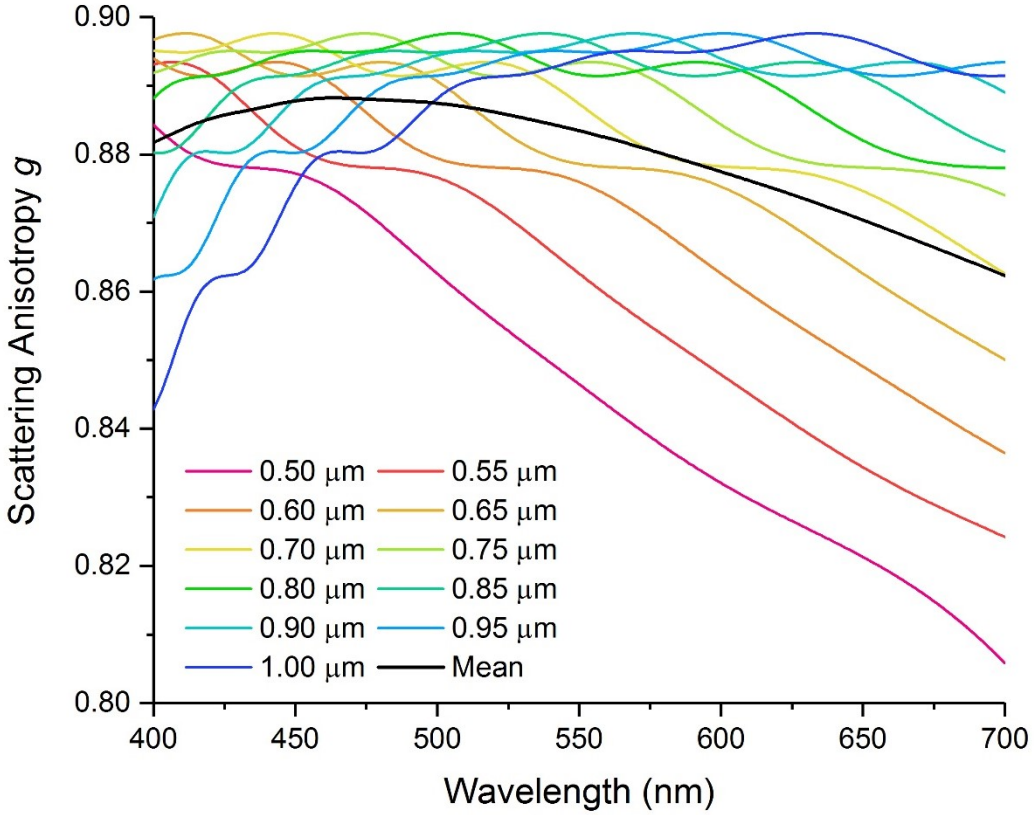

Figure 28. Scattering anisotropy *g* as calculated from Mie theory for Al_2O_3 spheres of various diameters in PDMS.

The optical properties of bloodless dermis were well-represented with a particular mixture of MF42 and 0.5 µm – 1 µm Al_2O_3 particles in PDMS, with the exception of a *g* value that cannot be confidently calculated due to the scattering properties of MF42 in addition to the known properties of the Al_2O_3. While the exact optical properties of the various epidermis tones mentioned in Table 8 were not specifically achieved, phantom materials with a wide variety of

optical properties that fall within the range set out by the three example epidermis tones were fabricated and characterized. These phantom materials are summarized in Table 10, Table 11, and Table 12.

Table 10. Optical properties of various concentrations of 0.5 µm – 1 µm Al_2O_3 particles and MF42 in PDMS with very small μ_a.

Concentration of Al_2O_3 (mg/g PDMS)	**Concentration of MF42 (mg/g PDMS)**	**μ_a (cm^{-1}) at 525 nm**	**μ_s' (cm^{-1}) at 525 nm**
12.46	0.94	0	14.82
18.28	0.73	0	31.94
24.34	0.90	0.2994	39.83
30.91	0.68	0.3648	44.04
12.63	1.21	0	17.97
18.11	1.36	0.1786	32.59
23.91	1.37	0.3825	41.08
31.34	1.22	0.4203	48.59
12.32	1.85	0.4445	17.85
18.72	1.79	0.0167	31.57
23.74	1.67	0.2337	36.48
31.03	1.68	0.2916	45.40
12.26	2.00	0.1494	17.11
18.91	2.09	0.2867	34.44
24.70	2.16	0.4916	40.04
31.27	2.19	0.5995	51.27

Table 11. Optical properties of various concentrations of 0.5 µm – 1 µm Al_2O_3 particles and MF42 in PDMS with μ_a near that of bloodless dermis. Bold: the mixture closest matching those of bloodless dermis model B.

Concentration of Al_2O_3 (mg/g PDMS)	**Concentration of MF42 (mg/g PDMS)**	**μ_a (cm^{-1}) at 525 nm**	**μ_s' (cm^{-1}) at 525 nm**
26.17	4.04	1.517	49.50
35.36	3.52	1.513	62.65
48.45	4.22	1.684	76.44
57.99	3.66	1.478	96.74
25.89	5.24	1.905	50.56
37.35	5.56	1.432	65.09
46.13	5.11	1.471	72.05
56.21	5.45	1.827	84.08
27.07	6.64	1.541	44.85
36.93	6.58	1.952	70.44
47.70	7.09	2.273	79.09
55.93	6.48	2.281	103.6
23.30	**7.85**	**2.778**	**48.84**
36.43	8.50	2.574	63.88
46.36	8.59	2.719	83.72
56.51	8.43	3.090	101.4

Table 12. Optical properties of various concentrations of 0.5 µm – 1 µm Al_2O_3 particles and India ink in PDMS.

Concentration of Al_2O_3 (mg/g PDMS)	**Concentration of India Ink (µL/g PDMS)**	**μ_a (cm^{-1}) at 525 nm**	**μ_s' (cm^{-1}) at 525 nm**
11.22	3.15	4.878	15.04
11.30	3.17	3.805	14.37
16.73	1.75	1.818	24.27
16.28	15.78	28.15	7.712
68.85	2.15	4.162	107.0
12.50	2.06	1.728	13.53
14.00	2.09	3.175	17.05
15.29	2.09	5.189	21.33
12.54	2.46	1.890	10.32
13.92	2.46	3.026	13.98
15.21	2.45	3.104	15.95
12.56	2.81	3.333	13.42
13.86	2.81	3.871	12.92
15.19	2.80	1.921	12.66
44.43	10.62	12.13	48.40
55.79	1.33	1.006	52.06

CHAPTER VI

CONCLUSIONS AND FUTURE WORK

The utility of phantoms comes from their ability to test devices without major physiological interference or unpredictability, and they should be used to model something that is well-understood but needs to be simplified or controlled for initial device evaluations to run more smoothly. Since reports in the literature show such large ranges of tissue optical properties and of tissue anatomy descriptions, along with uncertainty regarding the source of the green reflection PPG signal, it is difficult to create computational or physical models that adequately describe *in vivo* conditions. However, even though the anatomical models that formed the basis for this work do not adequately describe the nature of photon transport in cutaneous tissue, the phantom methods described herein do show promise toward being able to model the tissue optics of the wrist in regard to PPG-based monitoring. This work has shown that a complex model of several tissue layers' microcirculation can be simplified while still retaining a similar captured reflectance signal. This means that the fabrication of a phantom model for laboratory use can be performed much more easily than what would be required if the full spatial parameters of the tissue, including location-dependent blood content and another microfeatures, were required to be maintained. As improved anatomical models of the skin become available, the simplified computational models and their phantom counterparts can be adapted to match the properties of the better-understood anatomy so that the testing of devices can be made more accurate with respect to the true *in vivo* circumstances. Such improved phantoms will then be able to be used as black box models to evaluate the hardware and software of reflection PPG sensors to aid in the design and testing of products.

The work in this area has several opportunities to grow. The mechanical properties of the phantoms, particularly the Young's modulus, can be optimized in order to realistically model the blood pressure pulse *in vitro* for a dual-modality optical and mechanical phantom. The optics of the phantoms can be combined with materials science or mechanical engineering principles to yield a model that not only describes light transport throughout the cardiac cycle but that also emulates the behavior of tissue in certain cardiovascular conditions or disease states, such as arteriosclerosis or hypertension. This would, for example, allow an investigation into how PPG signals on certain medical patients may differ and for those differences to be tied back to certain parameters as a confirmation of what computational modeling may show, thus improving medical device performance. In addition, this work can be expanded to optimize for additional wavelengths and other illumination and detector geometries and layouts.

A phantom design based on anatomical models but with a simplified geometry was described in the previous chapter. This family of phantoms takes the anatomy and physiology of the cutaneous vasculature into account more than the single-vessel phantoms did. While these phantoms have not been fabricated, the procedure to do so would be very similar to that of the single-vessel phantoms. Rather than embedding a metal rod during curing and removing it afterward, a sheet of appropriate thickness should be embedded into the bloodless dermis. Specifically, the bottom layer of dermis should be cured first. Then, the sheet should be placed flat on top of the cured layer, and more uncured dermis should be poured over it. This step can be done on a scale to ensure the proper amount of PDMS is added, since Sylgard 184 has a density of ~1 g/mL. After the top layer of dermis has cured, then the epidermis layer can be added. This step should again be done with a scale. The dermis phantom should be weighed and then dipped into a container filled shallowly with uncured epidermis phantom. It should be dipped again if its new

weight does not indicate enough epidermis phantom has been added to achieve the appropriate thickness of ~81 μm, or excess can be wiped off if its weight is too high. Finally, the whole material should be cured. Afterward, the sheet can be removed to leave a hollow layer that can be filled with blood phantom and connected to a pump via tubing. Since the Young's modulus of PDMS is affected by the time and temperature at which it is cured,[84] this parameter can be tuned to allow for the appropriate cross-sectional distension during pumping and resultant pulsatile reflectance.

REFERENCES

1. Kantar Worldpanel ComTech, "Nearly 16% of US consumers and 9% in EU4 now own wearables," Kantar Worldpanel (2017).

2. Fitbit, Inc., "Form 10-K – For the fiscal year ended December 31, 2016," United States Securities and Exchange Commission, Washington, D.C. (2017).

3. "General wellness: Policy for low risk devices – Guidance for industry and Food and Drug Administration staff," United States Department of Health and Human Services, Food and Drug Administration (2016).

4. F. Lombardi, A. Porta, M. Marzegalli, S. Favale, M. Santini, A. Vincenti, and A. De Rosa, "Heart rate variability patterns before ventricular tachycardia onset in patients with an implantable cardioverter defibrillator," *The American Journal of Cardiology* **86**(9), 959-963 (2000).

5. P. Harris and D. Lysitsas, "Ventricular arrhythmias and sudden cardiac death," *BJA Education* **16**(7), 221-229 (2016).

6. F. Lombardi, T. H. Mäkikallio, R. J. Myerburg, and H. V. Huikuri, "Sudden cardiac death: Role of heart rate variability to identify patients at risk," *Cardiovascular Research* **50**(2), 210-217 (2001).

7. A. Baldzizhar, E. Manuylova, R. Marchenko, Y. Kryvalap, and M. G. Carey, "Ventricular tachycardias: Characteristics and management," *Critical Care Nursing Clinics of North America* **28**(3), 317-329 (2016).

8. L. Cadmus-Bertram, R. Gangnon, E. J. Wirkus, K. M. Thraen-Borowski, and J. Gorzelitz-Liebhauser, "The accuracy of heart rate monitoring by some wrist-worn activity trackers," *Annals of Internal Medicine* **166**(8), 610-612 (2017).

9. R. Wang, G. Blackburn, M. Desai, D. Phelan, L. Gillinov, P. Houghtaling, and M. Gillinov, "Accuracy of wrist-worn heart rate monitors," *JAMA Cardiology* **2**(1), 104-106 (2017).

10. Association for the Advancement of Medical Instrumentation, "Cardiac monitors, heart rate meters, and alarms," Association for the Advancement of Medical Instrumentation, Arlington, VA (2002).

11. J. Farmer, "Blood oxygen measurement," in *Design of Pulse Oximeters*, J. G. Webster, Ed., 21-39, Institute of Physics Publishing, Bristol, United Kingdom (1997).

12. S. A. Prahl, "Tabulated molar extinction coefficient for hemoglobin in water," 1998, http://www.omlc.org/spectra/hemoglobin/summary.html (9 July 2018).

13. M. Kumar, A. Veeraraghavan, and A. Sabharwal, "DistancePPG: Robust non-contact vital signs monitoring using a camera," *Biomedical Optics Express* **6**(5), 1565-1588 (2015).

14. N. D. Giardino, P. M. Lehrer, and R. Edelberg, "Comparison of finger plethysmograph to ECG in the measurement of heart rate variability," *Psychophysiology* **39**(2), 246-253 (2002).

15. E. Gil, M. Orini, R. Bailón, J. M. Vergara, L. Mainardi, and P. Laguna, "Photoplethysmography pulse rate variability as a surrogate measurement of heart rate variability during non-stationary conditions," *Physiological Measurement* **31**(9), 1271-1290 (2010).

16. C. S. Bulte, S. W. Keet, C. Boer, and R. A. Bouwman, "Level of agreement between heart rate variability and pulse rate variability in healthy individuals," *European Journal of Anaesthesiology* **28**(1), 34-38 (2011).

17. N. Pinheiro, R. Couceiro, J. Henriques, J. Muehlsteff, I. Quintal, L. Gonçalves, and P. Carvalho, "Can PPG be used for HRV analysis?," *Annual International Conference of the IEEE Engineering in Medicine and Biology Society (EMBC)* 2945-2949 (2016).

18. S. S. Thomas, V. Nathan, C. Zong, K. Soundarapandian, X. Shi, and R. Jafari, "BioWatch: A noninvasive wrist-based blood pressure monitor that incorporates training techniques for posture and subject variability," *IEEE Journal of Biomedical and Health Informatics* **20**(5), 1291-1300 (2016).

19. G. Zhang, M. Gao, D. Xu, N. B. Olivier, and R. Mukkamala, "Pulse arrival time is not an adequate surrogate for pulse transit time as a marker of blood pressure," *Journal of Applied Physiology* **111**(6), 1681-1686 (2011).

20. R. Mukkamala, J. O. Hahn, O. T. Inan, L. K. Mestha, C. S. Kim, H. Toreyin, and S. Kyal, "Toward ubiquitous blood pressure monitoring via pulse transit time: Theory and practice," *IEEE Transactions on Biomedical Engineering* **62**(8), 1879-901 (2015).

21. T. Pereira, C. Correia, and J. Cardoso, "Novel methods for pulse wave velocity measurement," *Journal of Medical and Biological Engineering* **35**(5), 555-565 (2015).

22. J. R. Levick, *An Introduction to Cardiovascular Physiology*, 4th ed., Arnold, London, United Kingdom (2003).

23. T. J. Akl, T. J. King, R. Long, M. N. Ericson, M. A. Wilson, M. J. McShane, and G. L. Coté, "*In vitro* performance of a perfusion and oxygenation optical sensor using a unique liver phantom," R. J. Nordstrom and G. L. Coté, Eds., *Optical Diagnostics and Sensing XII: Toward Point-of-Care Diagnostics; and Design and Performance Validation of Phantoms Used in Conjunction with Optical Measurement of Tissue IV* 822904 (2012).

24. M. B. Robinson, R. J. Butcher, M. A. Wilson, M. N. Ericson, and G. L. Coté, "In-silico and in-vitro investigation of a photonic monitor for intestinal perfusion and oxygenation," *Biomedical Optics Express* **8**(8), 3714-3734 (2017).

25. M. S. Durkee, F. Nooshabadi, J. D. Cirillo, and K. C. Maitland, "Optical model of the murine lung to optimize pulmonary illumination," *Journal of Biomedical Optics* **23**(7), 071208 (2018).

26. C. F. Bohren and D. R. Huffman, *Absorption and Scattering of Light by Small Particles*, John Wiley & Sons, Inc., New York, NY (1983).

27. V. Tuchin, *Tissue Optics: Light Scattering Methods and Instruments for Medical Diagnostics*, 3rd ed., SPIE, Bellingham, WA (2015).

28. W. M. Star, J. P. A. Marijnissen, and M. J. C. van Gemert, "Light dosimetry in optical phantoms and in tissues: I. Multiple flux and transport theory," *Physics in Medicine & Biology* **33**(4), 437-454 (1988).

29. R. Graaff, J. G. Aarnoudse, J. R. Zijp, P. M. A. Sloot, F. F. M. de Mul, J. Greve, and M. H. Koelink, "Reduced light-scattering properties for mixtures of spherical particles: a simple approximation derived from Mie calculations," *Applied Optics* **31**(10), 1370-1376 (1992).

30. T. Lister, P. A. Wright, and P. H. Chappell, "Optical properties of human skin," *Journal of Biomedical Optics* **17**(9), 090901 (2012).

31. L. Wang, S. L. Jacques, and L. Zheng, "MCML—Monte Carlo modeling of light transport in multi-layered tissues," *Computer Methods and Programs in Biomedicine* **47**(2), 131-146 (1995).

32. L. Wang and S. L. Jacques, "Monte Carlo modeling of light transport in multi-layered tissues in Standard C," University of Texas M. D. Anderson Cancer Center (1995).

33. S. A. Prahl, M. J. van Gemert, and A. J. Welch, "Determining the optical properties of turbid media by using the adding–doubling method," *Applied Optics* **32**(4), 559-568 (1993).

34. Quest Diagnostics, "Hemoglobin," *Test Center*, 2007, https://www.questdiagnostics.com/testcenter/TestDetail.action?ntc=510 (9 July 2018).

35. J. M. Otto, J. O. M. Plumb, E. Clissold, S. B. Kumar, D. J. Wakeham, W. Schmidt, M. P. W. Grocott, T. Richards, and H. E. Montgomery, "Hemoglobin concentration, total hemoglobin mass and plasma volume in patients: Implications for anemia," *Haematologica* **102**(9), 1477-1485 (2017).

36. H. P. Erickson, "Size and shape of protein molecules at the nanometer level determined by sedimentation, gel filtration, and electron microscopy," *Biological Procedures Online* **11**, 32-51 (2009).

37. D. J. Faber, M. C. G. Aalders, E. G. Mik, B. A. Hooper, M. J. C. van Gemert, and T. G. van Leeuwen, "Oxygen saturation-dependent absorption and scattering of blood," *Physical Review Letters* **93**(2), 028102 (2004).

38. A. Nahmad-Rohen, H. Contreras-Tello, G. Morales-Luna, and A. García-Valenzuela, "On the effective refractive index of blood," *Physica Scripta* **91**(1), 015503 (2016).

39. A. N. Bashkatov, E. A. Genina, V. I. Kochubey, and V. V. Tuchin, "Optical properties of human skin, subcutaneous and mucous tissues in the wavelength range from 400 to 2000 nm," *Journal of Physics D: Applied Physics* **38**(15), 2543-2555 (2005).

40. A. N. Bashkatov, E. A. Genina, and V. V. Tuchin, "Tissue optical properties," in *Handbook of Biomedical Optics*, D. A. Boas, C. Pitris, and N. Ramanujam, Eds., 67-100, CRC Press, Boca Raton, FL (2011).

41. E. K. Chan, B. Sorg, D. Protsenko, M. O'Neil, M. Motamedi, and A. J. Welch, "Effects of compression on soft tissue optical properties," *IEEE Journal of Selected Topics in Quantum Electronics* **2**(4), 943-950 (1996).

42. M. Lualdi, A. Colombo, B. Farina, S. Tomatis, and R. Marchesini, "A phantom with tissue-like optical properties in the visible and near infrared for use in photomedicine," *Lasers in Surgery and Medicine* **28**(3), 237-243 (2001).

43. S. Prahl, "Everything I think you should know about inverse adding-doubling," Oregon Institute of Technology, Wilsonville, OR (2011).

44. S. Laurent, X. Girerd, J. J. Mourad, P. Lacolley, L. Beck, P. Boutouyrie, J. P. Mignot, and M. Safar, "Elastic modulus of the radial artery wall material is not increased in patients with essential hypertension," *Arteriosclerosis, Thrombosis, and Vascular Biology* **14**(7), 1223-1231 (1994).

45. D. Lee, J. Y. Kim, H. S. Kim, K. C. Lee, S. J. Lee, and H. J. Kwak, "Ultrasound evaluation of the radial artery for arterial catheterization in healthy anesthetized patients," *Journal of Clinical Monitoring and Computing* **30**(2), 215-219 (2016).

46. R. R. Anderson and J. A. Parrish, "Optical properties of human skin," in *The Science of Photomedicine*, J. D. Regan and J. A. Parrish, Eds., 147-194, Springer, Boston, MA (1982).

47. G. Zonios, J. Bykowski, and N. Kollias, "Skin melanin, hemoglobin, and light scattering properties can be quantitatively assessed *in vivo* using diffuse reflectance spectroscopy," *Journal of Investigative Dermatology* **117**(6), 1452-1457 (2001).

48. J. L. Reuss and D. Siker, "The pulse in reflectance pulse oximetry: Modeling and experimental studies," *Journal of Clinical Monitoring and Computing* **18**(4), 289-299 (2004).

49. J. L. Reuss, "Multilayer modeling of reflectance pulse oximetry," *IEEE Transactions on Biomedical Engineering* **52**(2), 153-159 (2005).

50. I. V. Meglinski and S. J. Matcher, "Quantitative assessment of skin layers absorption and skin reflectance spectra simulation in the visible and near-infrared spectral regions," *Physiological Measurement* **23**(4), 741-753 (2002).

51. I. V. Meglinski and S. J. Matcher, "Computer simulation of the skin reflectance spectra," *Computer Methods and Programs in Biomedicine* **70**(2), 179-186 (2003).

52. T. J. Ryan, "Cutaneous circulation," in *Physiology, Biochemistry, and Molecular Biology of the Skin*, L. A. Goldsmith, Ed., 1019-1084, Oxford University Press, New York, NY (1991).

53. K. S. Stenn, "The skin," in *Cell and Tissue Biology: A Textbook of Histology*, L. Weiss, Ed., 539-572, Urban & Schwarzenberg, Inc., Baltimore, MD (1988).

54. I. M. Braverman, "The cutaneous microcirculation," *Journal of Investigative Dermatology Symposium Proceedings* **5**(1), 3-9 (2000).

55. I. M. Braverman, "Ultrastructure and organization of the cutaneous microvasculature in normal and pathologic states," *Journal of Investigative Dermatology* **93**(2, Supplement), 2S-9S (1989).

56. J. T. Whitton and J. Everall, "The thickness of the epidermis," *British Journal of Dermatology* **89**(5), 467-476 (1973).

57. F. Mahler, M. H. Muheim, M. Intaglietta, A. Bollinger, and M. Anliker, "Blood pressure fluctuations in human nailfold capillaries," *American Journal of Physiology-Heart and Circulatory Physiology* **236**(6), H888-H893 (1979).

58. A. C. Shore, D. D. Sandeman, and J. E. Tooke, "Capillary pressure, pulse pressure amplitude, and pressure waveform in healthy volunteers," *American Journal of Physiology-Heart and Circulatory Physiology* **268**(1), H147-H154 (1995).

59. L. H. Smaje, P. A. Fraser, and G. Clough, "The distensibility of single capillaries and venules in the cat mesentery," *Microvascular Research* **20**(3), 358-370 (1980).

60. G. S. Kassab, K. N. Le, and Y.-C. B. Fung, "A hemodynamic analysis of coronary capillary blood flow based on anatomic and distensibility data," *American Journal of Physiology-Heart and Circulatory Physiology* **277**(6), H2158-H2166 (1999).

61. W. Montagna and P. F. Parakkal, *The Structure and Function of Skin*, 3rd ed., Academic Press, Inc., New York, NY (1974).

62. Y. Behzadi and T. T. Liu, "An arteriolar compliance model of the cerebral blood flow response to neural stimulus," *NeuroImage* **25**(4), 1100-1111 (2005).

63. G. F. Odland, "Structure of the skin," in *Physiology, Biochemistry, and Molecular Biology of the Skin*, L. A. Goldsmith, Ed., 3-62, Oxford University Press, New York, NY (1991).

64. B. Fagrell, "Microcirculation of the skin," in *The Physiology and Pharmacology of the Microcirculation*, N. A. Mortillaro, Ed., 133-180, Academic Press, Inc., Orlando, FL (1984).

65. E. M. Landis, "Micro-injection studies of capillary blood pressure in human skin," *Heart* **15**, 209-228 (1930).

66. E. Kaxiras, A. Tsolakidis, G. Zonios, and S. Meng, "Structural model of eumelanin," *Physical Review Letters* **97**(21), 218102 (2006).

67. S. L. Jacques, "Skin optics," *Oregon Medical Laser Center News*, 1998, http://omlc.ogi.edu/news/jan98/skinoptics.html (10 January 2018).

68. J. R. Mourant, J. P. Freyer, A. H. Hielscher, A. A. Eick, D. Shen, and T. M. Johnson, "Mechanisms of light scattering from biological cells relevant to noninvasive optical-tissue diagnostics," *Applied Optics* **37**(16), 3586-3593 (1998).

69. L. Bozec and M. Odlyha, "Thermal denaturation studies of collagen by microthermal analysis and atomic force microscopy," *Biophysical Journal* **101**(1), 228-236 (2011).

70. C. A. Miles and A. J. Bailey, "Thermal denaturation of collagen revisited," *Proceedings of the Indian Academy of Sciences (Chemical Sciences)* **111**(1), 71-80 (1999).

71. E. Salomatina, B. Jiang, J. Novak, and A. N. Yaroslavsky, "Optical properties of normal and cancerous human skin in the visible and near-infrared spectral range," *Journal of Biomedical Optics* **11**(6), 064026 (2006).

72. S. L. Jacques, "Skin optics summary," *Oregon Medical Laser Center News*, 1998, https://omlc.org/news/jan98/skinoptics.html (10 July 2018).

73. R. Marchesini, C. Clemente, E. Pignoli, and M. Brambilla, "Optical properties of *in vitro* epidermis and their possible relationship with optical properties of *in vivo* skin," *Journal of Photochemistry and Photobiology B: Biology* **16**(2), 127-140 (1992).

74. M. J. C. van Gemert, S. L. Jacques, H. J. C. M. Sterenborg, and W. M. Star, "Skin optics," *IEEE Transactions on Biomedical Engineering* **36**(12), 1146-1154 (1989).

75. S. Wan, R. R. Anderson, and J. A. Parrish, "Analytical modeling for the optical properties of the skin with *in vitro* and *in vivo* applications," *Photochemistry and Photobiology* **34**(4), 493-499 (1981).

76. W. Verkruysse, J. W. Pickering, J. F. Beek, M. Keijzer, and M. J. van Gemert, "Modeling the effect of wavelength on the pulsed dye laser treatment of port wine stains," *Applied Optics* **32**(4), 393-398 (1993).

77. M. J. C. van Gemert, J. W. Pickering, and A. J. Welch, "Modeling laser treatment of port-wine stains," in *Management and Treatment of Benign Cutaneous Vascular Lesions*, O. T. Tan, Ed., 24-47, Lea & Febiger, Philadelphia, PA (1992).

78. S. A. Prahl, *Light Transport in Tissue,* Department of Biomedical Engineering, University of Texas at Austin, Austin, TX (1988).

79. R. R. Anderson, J. Hu, and J. A. Parrish, "Optical radiation transfer in the human skin and applications in *in vivo* remittance spectroscopy," in *Bioengineering and the Skin*, R. Marks and P. A. Payne, Eds., 253-265, Springer, Dordrecht, the Netherlands (1981).

80. S. L. Jacques, C. Alter, and S. A. Prahl, "Angular dependence of HeNe laser light scattering by human dermis," *Lasers in the Life Sciences* **1**(4), 309-333 (1987).

81. A. A. Kamshilin, E. Nippolainen, I. S. Sidorov, P. V. Vasilev, N. P. Erofeev, N. P. Podolian, and R. V. Romashko, "A new look at the essence of the imaging photoplethysmography," *Scientific Reports* **5**, 10494 (2015).

82. I. S. Sidorov, R. V. Romashko, V. T. Koval, R. Giniatullin, and A. A. Kamshilin, "Origin of infrared light modulation in reflectance-mode photoplethysmography," *PLOS ONE* **11**(10), e0165413 (2016).

83. A. A. Kamshilin and N. B. Margaryants, "Origin of photoplethysmographic waveform at green light," *Physics Procedia* **86**, 72-80 (2017).

84. H. Hocheng, C.-M. Chen, Y.-C. Chou, and C.-H. Lin, "Study of novel electrical routing and integrated packaging on bio-compatible flexible substrates," *Microsystem Technologies* **16**(3), 423-430 (2009).

85. L. M. Bellan, E. A. Strychalski, and H. G. Craighead, "Nanochannels fabricated in polydimethylsiloxane using sacrificial electrospun polyethylene oxide nanofibers," *Journal of Vacuum Science & Technology B: Microelectronics and Nanometer Structures Processing, Measurement, and Phenomena* **26**(5), 1728-1731 (2008).

86. C. Moraes, J. M. Labuz, Y. Shao, J. Fu, and S. Takayama, "Supersoft lithography: Candy-based fabrication of soft silicone microstructures," *Lab on a Chip* **15**(18), 3760-3765 (2015).

87. L. M. Bellan, S. P. Singh, P. W. Henderson, T. J. Porri, H. G. Craighead, and J. A. Spector, "Fabrication of an artificial 3-dimensional vascular network using sacrificial sugar structures," *Soft Matter* **5**(7), 1354-1357 (2009).

88. K. D. Roe and T. P. Labuza, "Glass transition and crystallization of amorphous trehalose-sucrose mixtures," *International Journal of Food Properties* **8**(3), 559-574 (2005).

APPENDIX A

MATLAB CODE FOR PROCESSING MULTILAYERED MONTE CARLO SIMULATION OUTPUT FILES

The multilayered Monte Carlo simulator developed by Wang et al.[31] yields an output file that tabulates, among other output parameters, the diffuse reflectance at the surface of the tissue as a function of radial distance from the point illumination source and the relative absorption in the tissue as a function of radial distance from the point illumination source and of depth, which can be used to calculate the normalized fluence. In order to determine the total reflectance captured by the photodetector when considering the geometry of the optical components in Figure 14, the output file needed to be processed. Two processing functions were developed in MATLAB R2016b. "MCML_processing.m" reads in a multilayered Monte Carlo output file, parses it into separate optical parameters, and calls "Integrate_PD_light_pct.m" to calculate the total captured diffuse reflectance. "Integrate_PD_light_pct.m" evenly distributes the unity input power of the simulated point illumination source over the area of a finite-sized LED and integrates the diffuse reflectance over the area of the photodetector.

MCML_processing.m

```
function [rvals, zvals, PD_pct, Rd_r_pct, fluenceWW, transmittance_pct, R_specular_pct, ...
    absorbed_pct, A_L_pct, A_z_pct, Tt_r_pct] = MCML_processing(path_to_simulation_output_file)

% Copyright 2018 Kevin Robert Bellows
% Developed as a student in the Texas A&M University Department of Biomedical Engineering.

% This code is for importing and plotting data from an output file generated by the multilayered Monte
% Carlo simulator developed by Wang et al.:
% L. Wang, S. L. Jacques, and L. Zheng, "MCML—Monte Carlo modeling of light transport in multi-layered
% tissues," Computer Methods and Programs in Biomedicine 47(2), 131-146 (1995).

% This code was developed in MATLAB R2016b and may not work properly in other versions of the software,
% especially if MATLAB changes the way it handles blank lines in imported files. In version R2016b,
% blank lines are completely ignored, e.g. if lines 2 and 4 of an imported file have text and line 3 is
% blank, line 4 of the file will be considered to be line 3 by MATLAB.

% Input parameter:
% path_to_simulation_output_file: absolute path to the file to be processed (string)

% Output parameters:
% rvals:             vector of radial distances [cm] used for plotting fluence [W/W]
% zvals:             vector of depths [cm] used for plotting fluence [W/W]
% PD_pct:            total light [%] captured by the photodiode
% Rd_r_pct:          diffuse reflectance [%] as a function of radial distance (rvals) from the simulated
%                       point illumination source
% fluenceWW:         fluence [W/W] in the tissue
% transmittance_pct: total transmittance [%] through the tissue
% R_specular_pct:    specular reflectance [%]
% absorbed_pct:      total light [%] absorbed by the tissue
% A_L_pct:           light absorbed [%] in each layer
% A_z_pct:           light absorbed [%] at each depth (zvals)
% Tt_r_pct:          transmittance [%] at each rval
```

```
%% Initialize variables.
delimiter = '\t'; % file is tab-delimited
startRow_header = 12;
endRow_header = 14;

%% Format for each line of text:
%   column1: double (%f) / column2: double (%f) / column3: double (%f)
formatSpec = '%f%f%f%*s%*s%*s%[^\n\r]';

%% Open the text file.
fileID = fopen(path_to_simulation_output_file, 'r');

%% Read columns of data according to the format.
textscan(fileID, '%[^\n\r]', startRow_header-1, 'WhiteSpace', '', 'ReturnOnError', false);
header_data = textscan(fileID, formatSpec, endRow_header-startRow_header+1, 'Delimiter', delimiter, ...
    'EmptyValue', NaN, 'ReturnOnError', false, 'EndOfLine', '\r\n');

%% Close the text file.
fclose(fileID);

Nz = header_data{1}(2); % number of depth values
Nr = header_data{2}(2); % number of radial distance values
Na = header_data{3}(2); % number of angle values
dz = header_data{1}(1); % depth resolution [cm]
dr = header_data{2}(1); % radial resolution [cm]
NL = header_data{1}(3); % number of tissue layers

startRow_header2 = 17;
endRow_header2 = 17 + NL - 1;

%% Format for each line of text:
%   column5: double (%f) / column6: text (%s)
formatSpec = '%f%f%f%f%f%s%[^\n\r]';

%% Open the text file.
fileID = fopen(path_to_simulation_output_file, 'r');
```

```
%% Read columns of data according to the format.
textscan(fileID, '%[^\n\r]', startRow_header2-1, 'WhiteSpace', '', 'ReturnOnError', false);
header_data2 = textscan(fileID, formatSpec, endRow_header2-startRow_header2+1, 'Delimiter', ...
    delimiter, 'ReturnOnError', false, 'EndOfLine', '\r\n');

%% Close the text file.
fclose(fileID);

L_thicknesses = header_data2{5}';
L_names = header_data2{6};
for i = 1:length(L_names)
    L_names{i} = L_names{i}(3:end);
end

L_abs_coeffs = header_data2{2};
L_scatt_coeffs = header_data2{3};
z_abs_coeffs = zeros(Nz, 1); % Initializing absorption coefficient for each depth value (zvals)

for i = 1:NL
    indices = cumsum([0 round(L_thicknesses/dz)]) + 1;
    z_abs_coeffs(indices(i):indices(i+1)-1) = L_abs_coeffs(i)*ones(1, round(L_thicknesses(i)/dz));
end

firstRow = 1;
lastRow = 46 + 2*NL + Nz + 2*Nr + 2*Na + Nz*Nr/5 + 2*Nr*Na/5;
max_endRow = 2e6;

if lastRow > max_endRow
    endRow = [max_endRow * (1:floor(lastRow/max_endRow)), lastRow];
    startRow = [1, max_endRow * (1:floor(lastRow/max_endRow)) + 1];
else
    endRow = lastRow;
    startRow = firstRow;
end
```

```
%% Format for each line of text:
formatSpec = '%q%*s%*s%*s%*s%*s%[^\n\r]';

for i = 1:length(startRow)
    %% Open the text file.
    fileID = fopen(path_to_simulation_output_file, 'r');

    %% Read columns of data according to the format.
    textscan(fileID, '%[^\n\r]', startRow(i)-1, 'WhiteSpace', '', 'ReturnOnError', false);
    dataArray = textscan(fileID, formatSpec, endRow(i)-startRow(i)+1, 'Delimiter', delimiter, ...
        'EmptyValue', NaN,'ReturnOnError', false, 'EndOfLine', '\r\n');

    %% Close the text file.
    fclose(fileID);

    %% Allocate imported array to column variable names
    data{i} = dataArray{:, 1};
end

MCML_data = cat(1, data{:});

% Parse data
R_specular_pct = 100*str2double(MCML_data(19+NL));
absorbed_pct = 100*str2double(MCML_data(21+NL));
transmittance_pct = 100*str2double(MCML_data(22+NL));
A_L_pct = 100*str2double(string(MCML_data((24+NL) : (24+2*NL-1))));
A_z_pct = 100*str2double(string(MCML_data((25+2*NL) : (25+2*NL+Nz-1))));
Rd_r_pct = 100*str2double(string(MCML_data((26+2*NL+Nz) : (26+2*NL+Nz+Nr-1))));
Tt_r_pct = 100*str2double(string(MCML_data((28+2*NL+Nz+Nr+Na) : (28+2*NL+Nz+2*Nr+Na-1))));

A_rz_pct = MCML_data((35+2*NL+Nz+2*Nr+2*Na) : (35+2*NL+Nz+2*Nr+2*Na+Nz*Nr/5-1));
A_rz_pct = 100*str2num([A_rz_pct{:}]);
A_rz_pct = reshape(A_rz_pct, [Nz, Nr])';

fluenceWW = A_rz_pct/100./z_abs_coeffs';
```

```
%% Plot log10(normalized fluence) rz-projection
backslashes = strfind(path_to_simulation_output_file, '\');
fig_title = path_to_simulation_output_file((backslashes(end)+1):(end-4)); % File name without extension
fig_title = strrep(fig_title, '_', '\_'); % Make any underscores in file name show up properly instead
                                          %   of being interpreted as subscript formatting
figure;
fluenceplot = surf(dz*(1:Nz), dr*(1:Nr), log10(fluenceWW));
colormap(jet);
c = colorbar;
xlabel('Depth (cm)');
ylabel('Radial Distance (cm)');
c.Label.String = 'log_{10}Normalized Fluence (W/W * cm^{-2})';
title(fig_title);
fluenceplot.EdgeColor = 'none';
view(90, 90);

rvals = dr*(1:Nr);
zvals = dz*(1:Nz);

% Calculate percentage of illumination that reaches a photodiode
% For SVTronics AFE4403 Watch EVM, the parameters are:
sL = 0.03; % length of LED side [cm]
D  = 0.2;  % LED-photodiode separation (closest distance) [cm]
sP = 0.14; % length of photodiode side [cm]
dL_LED = 0.001; % size of one side of LED square grid element [cm]; size should be small

PD_pct = Integrate_PD_pct(sL, D, sP, Rd_r_pct, Nr, dr, dL_LED);

end
```

Integrate_PD_light_pct.m

```
function PD_pct = Integrate_PD_pct(sL, D, sP, Rd_r_pct, Nr, dr, dL_LED)

% Copyright 2018 Kevin Robert Bellows
% Developed as a student in the Texas A&M University Department of Biomedical Engineering.

% This code is called by "MCML_processing.m" in order to calculate the total reflectance captured by a
% photodiode when considering an LED and photodiode each with finite area.

% This code was developed in MATLAB R2016b.

% Input parameters:
% sL:       length of LED side [cm]
% D:        LED-photodiode separation (closest distance) [cm]
% sP:       length of photodiode side [cm]
% Rd_r_pct: diffuse reflectance [%] as a function of radial distance (rvals) from the simulated point
%               illumination source
% Nr:       number of radial grid values [dimensionless]
% dr:       radial resolution [cm]
% dL_Led:   length of one side of LED square section [cm]

% Output parameter:
% PD_pct: total light [%] captured by the photodiode

num_angles = 1000;
theta = (1:num_angles)/num_angles*(2*pi);

% Define border of photodiode
PD_xmin = sL + D;
PD_xmax = sL + D + sP;
PD_ymin = 0;
PD_ymax = sP;

PD_pct = 0; % Initialize variable
num_LED_sections = length((0:round(sL/dL_LED-1)) * dL_LED + dL_LED/2)^2;
```

```
for a = (0:round(sL/dL_LED-1)) * dL_LED + dL_LED/2
    for b = (0:round(sL/dL_LED-1)) * dL_LED + dL_LED/2
        for i = 1:Nr
            r = (i-0.5) * dr; % Radial coordinate of grid element i
            x = a + r*cos(theta); % Convert polar coordinates to Cartesian coordinates
            y = b + r*sin(theta); % Convert polar coordinates to Cartesian coordinates

            % Determine angular fraction of the current grid element that is contained within the
            %   photodiode area
            circle_fraction(i) = sum(x > PD_xmin & x < PD_xmax & y > PD_ymin & y < PD_ymax)/num_angles;

            % Add the current grid element's captured reflectance to a running total:
            % total reflectance per area in grid element * area of grid element * angular fraction of
            %   grid element contained within photodiode area / number of LED sections (to maintain a
            %   total input power of unity)
            PD_pct = PD_pct + Rd_r_pct(i) * pi * dr^2 * (2*i-1) * circle_fraction(i) / num_LED_sections;
        end
    end
end

end
```

APPENDIX B

EMBEDDING OF MICROVESSELS WITHIN POLYDIMETHYLSILOXANE PHANTOMS

Attempts to fabricate a microvasculature phantom were made. Other researchers have demonstrated a method of embedding sacrificial microfibers within polymers and then removing them to leave behind microchannels for fluid to flow through.[85] In particular, sugar[86] and cotton candy[87] have been used as a sacrificial material. In this work, cotton candy was made with a cotton candy machine (Nostalgia Electrics, Oxnard, CA) by heating either table sugar or turbinado sugar until it liquefied and using a motor to spin it out of small holes. As the substance cooled while traveling through the air, it quickly solidified and formed glassy fibers. However, if the substance was too hot before being spun with the motor, then it would not solidify before hitting the walls of the collecting bowl. In this case, instead of fibers forming, clumps would form on the walls of the bowl. Additionally, the speed of the rotation was affected by how long the heater had been heating the spinning element.

The cotton candy needed to be handled extremely gently, otherwise it would form aggregates, rather than staying as discrete fibers. Additionally, the cotton candy would sometimes shrivel up inside the PDMS during the curing process. Curing at lower temperatures or even at room temperature sometimes prevented this from happening. However, humidity and temperature have been shown to affect the shelf life of cotton candy.[88] Since this fabrication problem was likely humidity-dependent, the results with regard to this were inconsistent.

When fabrication was successful, meaning the cotton candy stayed in or near its original geometry throughout the curing process, the next step was to remove the sacrificial fibers from the PDMS. This was done by soaking the material in DI H_2O and either leaving it to sit or placing it

in a sonicator to help break up the fibers. While UV-vis absorbance spectroscopy of the soaking fluid showed that all of the fiber mass eventually came out of the PDMS, there was still difficulty in producing flow through the network, specifically if the fibers did not aggregate before the polymer had finished curing. Since DI H_2O can pass through PDMS, it is possible that the fibers were being dissolved and passing through the PDMS walls in solution rather than through microchannels left by more exterior fibers that had already dissolved. This meant there may have been a lack of confluence, so flow was not possible without an immense driving pressure, which would invariably cause a tubing connection to break instead of generating flow through the material. Alternatively, the lack of confluence could have resulted from certain areas of microchannels sealing shut due to the walls of the structures sticking together. When dye was injected directly into fibers in the center of the PDMS, it did spread to adjacent channels. However, when pressure was added in an attempt to flow the fluid through the channels to the outlet, the fluid instead traveled through portions of PDMS that had no microchannels, thus creating leaks.

If there was aggregation before or during the curing process, the features of the channels became much larger. While this was undesirable in terms of modeling the anatomical and physiological parameters of the cutaneous vasculature, it did allow for the channels to be filled with fluid much more easily, as seen in Figure 29. Since this is a widefield image as opposed to a confocal image, several axial planes are viewed as a superposition in a single two-dimensional image. Thus, the channels that are not perfectly parallel to the lateral direction are still fully visible. The PDMS in this image was clear for visualization purposes, rather than having its bulk optical properties tuned to those of bloodless dermis.

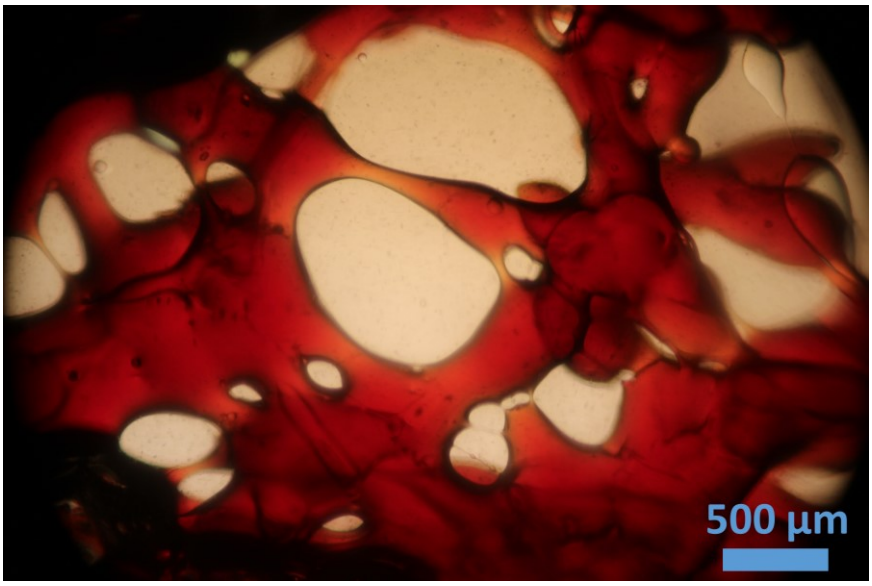

Figure 29. Brightfield image of a microfluidic network fabricated in PDMS with sacrificial cotton candy fibers and then filled with dye.

In addition to the difficulties with the curing process, the distribution of cotton candy in PDMS was difficult to control in terms of setting it equal to 5% v/v of the whole material. While untested, attempts to create an even more anatomically correct distribution of channels in what would ultimately be a dermis phantom would have been exceedingly difficult and impractical. Also, there was no way to control their length. Measurements in canine mesentery have shown capillaries to be approximately 400 µm long and small arteries and arterioles 1.5–2 mm.[22] However, the length of the fabricated cotton candy fibers was on the order of centimeters. Cutting them shorter after fabrication would have been difficult due to their tendency to aggregate with any applied pressure and due to the potential for creating a discontinuous network of fibers. As a result of these necessarily long fibers, their number density needed to be kept lower than what is seen of microvessels *in vivo* in order to maintain the proper amount of blood phantom per unit volume, once eventually filled. Since the resistance of a network increases with increased channel length and also with reduced number of parallel paths, the overall resistance of the microchannel

network was enormous when compared to the resistance of a microvasculature network *in vivo*, making establishing flow very difficult. Though flow has been achieved through microvessel networks fabricated with sacrificial cotton candy fibers in the past, there are many applications other than modeling the microvessel network to the cutaneous microvasculature, so the difficulties of changes in geometry inducing changes in number density of fibers was not a concern for many researchers.